J. Fluid Mech. (2013), *vol.* 716, *pp.* 280–315. © Cambridge University Press 2013
doi:10.1017/jfm.2012.547

Flows in annuli with longitudinal grooves

H. V. Moradi† and J. M. Floryan

Department of Mechanical and Materials Engineering, The University of Western Ontario, London, Ontario N6A 5B9, Canada

(Received 11 June 2012; revised 18 October 2012; accepted 2 November 2012)

Analysis of pressure losses in laminar flows through annuli fitted with longitudinal grooves has been carried out. The additional pressure gradient required in order to maintain the same flow rate in the grooved annuli, as well as in the reference smooth annuli, is used as a measure of the loss. The groove-induced changes can be represented as a superposition of a pressure drop due to a change in the average position of the bounding cylinders and a pressure drop due to flow modulations induced by the shape of the grooves. The former effect can be evaluated analytically while the latter requires explicit computations. It has been demonstrated that a reduced-order model is an effective tool for extraction of the features of groove geometry that lead to flow modulations relevant to drag generation. One Fourier mode from the Fourier expansion representing the annulus geometry is sufficient to predict pressure losses with an accuracy sufficient for most applications in the case of equal-depth grooves. It is shown that the presence of the grooves may lead to a reduction of pressure loss in spite of an increase of the surface wetted area. The drag-decreasing grooves are characterized by the groove wavenumber M/R_1 being smaller than a certain critical value, where M denotes the number of grooves and R_1 stands for the radius of the annulus. This number marginally depends on the groove amplitude and does not depend on the flow Reynolds number. It is shown that the drag reduction mechanism relies on the re-arrangement of the bulk flow that leads to the largest mass flow taking place in the area of the largest annulus opening. The form of the optimal grooves from the point of view of the maximum drag reduction has been determined. This form depends on the type of constraints imposed. In general, the optimal shape can be described using the reduced-order model involving only a few Fourier modes. It is shown that in the case of equal-depth grooves, the optimal shape can be approximated using a special form of trapezoid. In the case of unequal-depth grooves, where the groove depth needs to be determined as part of the optimization procedure, the optimal geometry, consisting of the optimal depth and the corresponding optimal shape, can be approximated using a delta function. The maximum possible drag reduction, corresponding to the optimal geometry, has been determined.

Key words: drag reduction, flow control

1. Introduction

The reduction of pressure losses associated with the movement of fluids through conduits has been of continuous interest from the very beginning of modern fluid

† Email address for correspondence: hvafadar@uwo.ca

https://doi.org/10.1017/jfm.2012.547 Published online by Cambridge University Press

mechanics. It has attracted even more attention in recent times due to an increase in the cost of energy and an interest in the reduction of environmental impact. Most of the fundamental work has been devoted to the classical canonical flows, e.g. pressure-driven flow either through a plane channel or through a circular pipe, kinematically driven flows (Couette flow) and various forms of boundary layers (the Blasius and the Falkner–Skan boundary layers). This work is focused another, less studied but nevertheless technologically important flow, i.e. a pressure-driven flow through an annulus formed by two concentric cylinders. This flow is widely encountered in petroleum engineering, heat exchangers, turbomachinery, fuels cells, aero-engines and various chemical industrial devices, where it has a significant impact on the efficiency of these devices. The question of stability of the annular flow and an understanding of the transition between the laminar and turbulent states represents a classical problem that has been studied for over fifty years. Heaton (2008) provides a summary of the current results in this area. The available transition prediction criteria are discussed by Dou, Khoo & Tsai (2010) and a new criterion is given using an energy gradient method (Dou 2011). A number of important variations of this flow have also been studied. Spiral flow occurs when one of the cylinders is subject to a rotation; a review of the relevant literature can be found in Cotrell & Pearlstein (2006). Recent results on the effects of eccentricity in the location of the cylinders are discussed by Walton, Labadin & Yiong (2010). Progress in modelling of the effects of surface roughness is well summarized by Valdes *et al.* (2007). The thread-annular flow found in minimally invasive surgical applications has been studied by Freai, Lüscher & Wintermantel (2000).

Variations in the structure of surface topography offers potential for improving the performance of flow systems, following examples found in biology (Jung & Bhushan 2010). The leaves of the lotus plant provide an example of a super-hydrophobic and low-drag surface. The special properties of this surface are associated with wax tubules that create a certain surface topography. Shark skin represents another good example of a low-drag surface. The skin is covered with very small tooth-like scales ribbed with longitudinal grooves which reduce the formation of vortices present on a smooth surface. It is known that surface topography (roughness) affects the form of turbulence (Jimenez 2004), it plays a large role in the laminar–turbulent transition (Floryan 2007) and it is used as a mixing augmentation technique in heat transfer (Valdes *et al.* 2007). The above examples illustrate the potential gains associated with the use of properly selected surface structures, assuming that one can achieve complete understanding of how these structures affect the flow.

The relationship between the surface topography and the form of movement of the adjacent fluid has been studied primarily in the context of analysis of surface roughness effects. This is one of the classical but, nevertheless, still not well understood topics in fluid dynamics. A large variety of possible responses, which depend on the details of roughness shape as well as on the flow conditions, prevents the lack of closure. The direct response can be measured in terms of resistance experienced by a flow. It had been thought, since the original experiments of Hagen (1854) and Darcy (1857), that roughness always increases this resistance. Nikuradse (1933) and Moody & Princeton (1944) introduced the concept of friction factor to quantify the drag and carried out extensive measurements. Their results demonstrate that roughness does not affect the laminar drag or, at least, the effect is too small to be measured using the techniques available at that time, and it always increases turbulent flow drag, with the increases being a function of the form of the roughness. Walsh (1980, 1983) contradicted these predictions by showing that roughness in the form

https://doi.org/10.1017/jfm.2012.547 Published online by Cambridge University Press

of streamwise grooves (riblets) can result in the reduction of turbulent drag. Recent interest in flows in micro-channels has led to a scrutiny of predictions regarding the laminar drag (Papautsky *et al.* 1999; Sobhan & Garimella 2001; Morini 2004; Sharp & Adrian 2004; Gamrat *et al.* 2008). To the best of our knowledge, only Valdes *et al.* (2007) have studied the effect of surface topography in annular flows.

Surface roughness can affect the flow dynamics indirectly by promoting/delaying the laminar–turbulent transition. Reynolds (1883) demonstrated that the presence of roughness always promotes transition. Recent evidence (Saric, Carrillo & Reibert 1998) demonstrates that roughness may play a stabilizing role. There is a large amount of relevant experimental data (Schlichting 1979) but meaningful progress in the understanding of the mechanics of flow response has been achieved only recently (Floryan 2007). A frequently used criterion (Morkovin 1990) for determination of the critical roughness size is that the roughness Reynolds number $Re_k = U_k k/\nu < 25$, where U_k is the undisturbed velocity at height k (the top of the roughness) and ν is the kinematic viscosity. This criterion does not account for the effect of roughness patterns when several roughness elements are present. A formal criterion for hydraulic smoothness in the case of distributed roughness states that such roughness is hydraulically active only when it is able to induce flow bifurcation (Floryan 2007); the relevant critical conditions can be identified using linear stability theory. The two-dimensional distributed roughness destabilizes travelling wave disturbances (Floryan 2005; Asai & Floryan 2006) and the two-dimensional waves remain critical (Floryan 2007). The same roughness can amplify disturbances in the form of streamwise vortices (Floryan 2007). The first bifurcation can lead either to the onset of travelling waves or streamwise vortices, depending on the roughness amplitude and wavenumber and on the flow Reynolds number. Similar flow responses have been found in Couette flow (Floryan 2002) and in the pressure-driven flow in a converging–diverging channel (Floryan 2003; Floryan & Floryan 2010). Roughness has been found to increase transient growth, with the streamwise vortices playing the role of the optimal disturbances (Szumbarski & Floryan 2006). The effect of roughness patterns on the flow stability has been analysed by Floryan & Asai (2011).

There is an uncountable number of geometric roughness forms and, thus, their modelling represents a challenge. Most of the experimental investigations used artificially created roughness forms, e.g. sets of cones, spheres, prisms, parallelepipeds, etc., with different spatial distributions (Schlichting 1979). Sandpaper with various grain sizes is an especially popular roughness representation due to the belief that it accounts for the 'uncountability'/randomness of roughness forms. Roughness properties have been most commonly measured using the equivalent sand roughness (Moody & Princeton 1944). A recent discussion of this and similar concepts is given in Herwig, Gloss & Wenterodt (2008). Numerical simulations require use of a well-defined geometry (Gamrat *et al.* 2008; Herwig *et al.* 2008). Only a finite number of configurations can be studied and this leads to uncertainty regarding the generality of the conclusions. The recent use of the reduced-order method (Floryan 1997) offers the potential for extraction of geometric features that are relevant for flow dynamics and elimination of the irrelevant details that clutter analysis and mask the relevant mechanisms. Use of such techniques may lead to general conclusions regarding the effects of roughness shape. The global shape properties can be extracted using projection of the surface geometry onto a convenient functional space, e.g. Fourier space, with the expectation that only a few leading Fourier modes matter. Such spectral models of surface geometry (Floryan 1997) have proved very successful as it has been demonstrated that, in many instances, it is sufficient to use only the leading

https://doi.org/10.1017/jfm.2012.547 Published online by Cambridge University Press

Fourier mode to capture the main physical processes with an accuracy sufficient for most applications (Floryan 2007).

The mechanisms of drag generation associated with surface corrugations have been clearly delineated only recently (Mohammadi & Floryan 2012). The shear drag is associated with surface-corrugation-induced changes in the wall shear, as well as an increase of the wetted area. The pressure form drag is associated with the mean pressure gradient driving the flow and the pressure interaction drag is generated by projection of the corrugation-modulated part of the pressure field on the surface geometry. The importance of pressure effects increases rapidly with the corrugation amplitude. Information about the types of drag and their dependence on the corrugation shape offers potential for identification of surface topographies that may result in a lower drag.

One particular form of surface topography, i.e. longitudinal grooves/ribs, commonly referred as riblets, has attracted attention due to their drag-reducing capabilities in turbulent flow regimes (Walsh 1980, 1983). Such grooves have a wavelength of the order of the viscous scale and lead to reduced shear drag through an interference with the turbulence production. The viscous regime of vanishing riblet spacing is well understood (Bechert & Bartenwerfer 1989; Lucini, Manzo & Pozzi 1991) and detailed measurements of the drag reduction for various shapes have been carried out by Bechert *et al.* (1997) and Frohnapfel, Jovanović & Delgado (2007). For larger riblets, the minimum drag is related to the breakdown of the viscous regime and this process is less understood (Garcia-Mayoral & Jimenez 2011). Laminar riblets have attracted less attention. Mohammadi & Floryan (2011) considered pressure-driven laminar flows and demonstrated the drag-reducing abilities of long-wavelength grooves associated with the redistribution of the bulk flow.

This work is focused on the analysis of laminar, pressure-driven flows in annuli fitted with longitudinal grooves of arbitrary shape and on the systematic search for the forms of such grooves that are able to reduce drag. The drag-reducing abilities are assessed by determining the additional pressure gradient required to maintain the same mass flow rate through the groove-fitted as well as through the smooth annuli. The problem formulation is given in § 2. Curvature effects are discussed in § 3, together with the form of the flow found in annuli with large radii. A spectrally accurate method of solution of the field equations for arbitrary geometric parameters is discussed in § 4. The groove-induced flow modifications are described in § 5. In particular, § 5.1 discusses the effects of changing the mean position of the cylinders, § 5.2 discusses the shape representation for arbitrary grooves and the reduced geometry models, § 5.3 describes the effects of the dominant parameters and § 5.4 discusses the mechanics of drag formation. Section 6 is focused on the identification of the optimal forms of the grooves which produce the maximum possible drag reduction. In particular, § 6.1 discusses the shapes determined with the equal-depth constraint (equal-depth grooves) and § 6.2 presents the shapes determined with the unequal-depth constraint (unequal-depth grooves). Section 7 provides a short summary of the main conclusions.

2. Problem formulation

Consider steady axial flow in an annulus bounded by two co-axial cylinders fitted with longitudinal grooves (figure 1). There are M identical grooves of an arbitrary

https://doi.org/10.1017/jfm.2012.547 Published online by Cambridge University Press

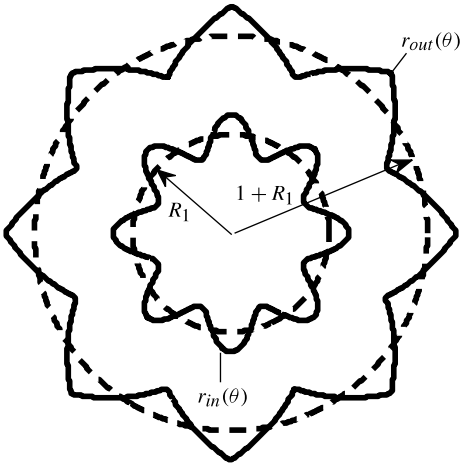


FIGURE 1. Sketch of the flow geometry: annulus with longitudinal grooves with an arbitrary geometry.

shape over the circumference and thus wall geometries can be expressed as

$$r_{in}(\theta) = R_1 + \sum_{n=-N_A}^{N_A} H_{in}^{(n)} \mathrm{e}^{\mathrm{i}nM\theta}, \quad r_{out}(\theta) = 1 + R_1 + \sum_{n=-N_A}^{N_A} H_{out}^{(n)} \mathrm{e}^{\mathrm{i}nM\theta}, \tag{2.1}$$

where R_1 and $1 + R_1$ are the radii of the smooth reference inner and outer cylinders, $H_{in}^{(n)} = H_{in}^{(-n)*}$, $H_{out}^{(n)} = H_{out}^{(-n)*}$ are the reality conditions, stars denote the complex conjugates, N_A is the number of Fourier modes required for description of the shape of the grooves, and all quantities have been scaled with the gap L between the reference cylinders as the length scale. Choice of $H_{in}^{(n)}$ and $H_{out}^{(n)}$ is restricted by the no-contact condition between the cylinders. It is worth noting that (2.1) provides a means to describe a wide class of annuli, while this analysis is focused on circular annuli fitted with grooves.

The flow is driven by a constant axial pressure gradient and this leads to a velocity field with the velocity vector having components $(v, 0, 0)$ in the (z, r, θ) directions. This field is completely described by the axial momentum equation in the form

$$\left(\frac{1}{r}\frac{\partial v}{\partial r} + \frac{\partial^2 v}{\partial r^2} + \frac{1}{r^2}\frac{\partial^2 v}{\partial \theta^2}\right) = Re\frac{\partial p}{\partial z}, \tag{2.2}$$

which has been scaled using the maximum of the axial velocity of the reference flow U_{max} as the velocity scale and ρU_{max}^2 as the pressure scale where ρ stands for the density. The Reynolds number is defined as $Re = U_{max}L/\nu$ where ν stands for the kinematic viscosity. The boundary conditions have the form

$$v(r, \theta) = 0 \quad \text{at } r = r_{in}(\theta) \text{ and } r = r_{out}(\theta). \tag{2.3}$$

The problem of determination of the effects of the grooves is posed as the problem of determination of an additional pressure gradient required in order to maintain the same flow rate in the grooved annulus as in the reference smooth annulus. This necessitates

https://doi.org/10.1017/jfm.2012.547 Published online by Cambridge University Press

introduction of the flow rate constraint in the form

$$Q = M \int_0^{2\pi/M} \int_{r_{in}(\theta)}^{r_{out}(\theta)} rv \, \mathrm{d}r \, \mathrm{d}\theta, \tag{2.4}$$

where Q is the known flow rate; this flow rate is equal to the flow rate in the corresponding smooth annulus.

The reference flow, i.e. flow in a smooth annulus, has velocity distribution, pressure gradient and flow rate expressed as (Tasos, Georgios & Andreas 1999)

$$v_0(r) = R_1^2[1 - (r/R_1)^2]/k_1 + k_2 \ln(r/R_1)/k_1, \tag{2.5}$$

$$\mathrm{d}p_0/\mathrm{d}z = -4/k_1 Re, \tag{2.6}$$

$$\begin{aligned} Q_0 = {} & 2\pi[(1+R_1)^2(R_1^2 - 2R_1 - 1 - k_2)/4 \\ & + k_2 (1+R_1)^2 \ln((1+R_1)/R_1)/2 + R_1^2(k_2 - 1)/4]/k_1, \end{aligned} \tag{2.7}$$

where $k_1 = R_1^2 - k_2 \ln R_1 + k_2/2[\ln(k_2/2) - 1]$ and $k_2 = (1 + 2R_1)/\ln[(1+R_1)/R_1]$. The maximum of v_0 occurs at $r = \sqrt{k_2/2}$ and this defines the velocity scale U_{max}.

3. Curvature effects

The magnitude of the annulus curvature is expressed in terms of its radius R_1. It is more convenient to analyse the relative importance of curvature effects by expressing the model equations using a boundary-oriented coordinate system (y, t), where y denotes the distance measured outward from the inner cylinder, i.e. $y = r - R_1$, and t stands for the arclength measured along the inner cylinder, i.e. $\theta = t/R_1$. Problem (2.2)–(2.4) takes the form

$$\left[\frac{R_1^{-1}}{1 + yR_1^{-1}} \frac{\partial v}{\partial y} + \frac{\partial^2 v}{\partial y^2} + \frac{1}{\left(1 + yR_1^{-1}\right)^2} \frac{\partial^2 v}{\partial t^2} \right] = Re \frac{\partial p}{\partial z}, \tag{3.1}$$

$$v(y, t) = 0 \quad \text{at } y = y_{in}(t) \text{ and } y = y_{out}(t), \tag{3.2}$$

$$Q = \alpha R_1 \int_0^{2\pi/\alpha} \int_{y_{in}(t)}^{y_{out}(t)} (y/R_1 + 1) v \, \mathrm{d}y \, \mathrm{d}t, \tag{3.3}$$

where

$$y_{in}(t) = \sum_{n=-N_A}^{N_A} H_{in}^{(n)} \mathrm{e}^{\mathrm{i}n\alpha t}, \quad y_{out}(t) = 1 + \sum_{n=-N_A}^{N_A} H_{out}^{(n)} \mathrm{e}^{\mathrm{i}n\alpha t}, \tag{3.4}$$

and $\alpha = M/R_1$ will be referred to as the groove wavenumber. The problems associated with the treatment of the boundary conditions on grooved surfaces are eliminated by introducing a transformation of the form

$$\xi = \alpha t, \quad \eta = 1 + 2[y - y_{out}(t)]\,[y_{out}(t) - y_{in}(t)]^{-1}, \tag{3.5}$$

which maps the solution domain onto a strip $\eta \in [-1, 1]$. The coordinate ξ is defined in such a way that it can play the role of a slow scale when $\alpha \to 0$. The problem expressed in the new coordinates takes the form

$$F_{A,1} \frac{\partial v}{\partial \eta} + F_{A,2} \frac{\partial^2 v}{\partial \eta^2} + F_{A,3} \frac{\partial^2 v}{\partial \eta \partial \xi} + F_{A,4} \frac{\partial^2 v}{\partial \xi^2} = Re \frac{\partial p}{\partial z}, \tag{3.6a}$$

https://doi.org/10.1017/jfm.2012.547 Published online by Cambridge University Press

$$v(\xi,\eta)=0 \quad \text{at } \eta=\mp 1, \tag{3.6b}$$

$$Q=0.5R_1\int_0^{2\pi}\int_{-1}^{1}[1+R_1^{-1}F(\eta,\xi)]v(\eta,\xi)f(\xi)\,\mathrm{d}\eta\,\mathrm{d}\xi, \tag{3.6c}$$

where the coefficients are presented in appendix A. It is convenient to carry out further discussion in the context of sinusoidal grooves placed on the inner cylinder, i.e.

$$y_{in}(t)=0.5S_{in}\cos(Mt/R_1), \quad y_{out}(t)=1, \tag{3.7}$$

where S_{in} is the top to bottom distance of the grooves. In the case of large R_1 it is possible to express the solution as asymptotic expansions of the form

$$v=\hat{v}_0+R_1^{-1}\hat{v}_1+O(R_1^{-2}), \quad p=\hat{p}_0+R_1^{-1}\hat{p}_1+O(R_1^{-2}). \tag{3.8}$$

It is further assumed that the number of grooves increases with R_1 so that the wavenumber M/R_1 remains $O(1)$. This process is not continuous, as only integer numbers of grooves are permitted. However, it is still possible to consider the limit $R_1\to\infty$. The flow rate can be expressed as

$$Q/2\pi R_1=\hat{Q}_0+R_1^{-1}\hat{Q}_1+O(R_1^{-2})=\tfrac{2}{3}+\tfrac{1}{3}R_1^{-1}+O(R_1^{-2}). \tag{3.9}$$

Expanding the coefficients, substituting (3.8) into (3.6) and retaining the terms of the two highest orders of magnitude results in the following problems:

$$O(1): \quad H_3(\eta,\xi)\frac{\partial\hat{v}_0}{\partial\eta}+[H_1^2(\eta,\xi)+H_2^2(\eta,\xi)]\frac{\partial^2\hat{v}_0}{\partial\eta^2}+2\alpha H_2(\eta,\xi)\frac{\partial^2\hat{v}_0}{\partial\eta\partial\xi}+\alpha^2\frac{\partial^2\hat{v}_0}{\partial\xi^2}=Re\frac{\partial\hat{p}_0}{\partial z}, \tag{3.10a}$$

$$\hat{Q}_0=\frac{1}{4\pi}\int_0^{2\pi}\int_{-1}^{1}\hat{v}_0(\eta)f(\xi)\,\mathrm{d}\eta\,\mathrm{d}\xi, \tag{3.10b}$$

$$\hat{v}_0(\eta)=0 \quad \text{at } \eta=\pm 1; \tag{3.10c}$$

$$O\left(R_1^{-1}\right): \quad [H_1(\eta,\xi)-2H_3(\eta,\xi)F(\eta,\xi)]\frac{\partial\hat{v}_0}{\partial\eta}+H_3(\eta,\xi)\frac{\partial\hat{v}_1}{\partial\eta}+[H_1^2(\eta,\xi)+H_2^2(\eta,\xi)]\frac{\partial^2\hat{v}_1}{\partial\eta^2}-2H_2^2(\eta,\xi)F(\eta,\xi)\frac{\partial^2\hat{v}_0}{\partial\eta^2}+2\alpha H_2(\eta,\xi)\frac{\partial^2\hat{v}_1}{\partial\eta\partial\xi}-4\alpha H_2(\eta,\xi)F(\eta,\xi)\frac{\partial^2\hat{v}_0}{\partial\eta\partial\xi}+\alpha^2\frac{\partial^2\hat{v}_1}{\partial\xi^2}-2\alpha^2F(\eta,\xi)\frac{\partial^2\hat{v}_0}{\partial\xi^2}=Re\frac{\partial\hat{p}_1}{\partial z}, \tag{3.11a}$$

$$\hat{Q}_1=\frac{1}{4\pi}\int_0^{2\pi}\int_{-1}^{1}[\hat{v}_0(\eta)F(\eta,\xi)+\hat{v}_1(\eta)]f(\xi)\,\mathrm{d}\eta\,\mathrm{d}\xi, \tag{3.11b}$$

$$\hat{v}_1(\eta)=0 \quad \text{at } \eta=\pm 1. \tag{3.11c}$$

Problem (3.10) describes the flow in a straight grooved channel studied by Mohammadi & Floryan (2011). Curvature enters the solution at $O(R_1^{-1})$. The effects of the grooves disappear in the limit $S_{in}\to 0$ and the above problems yield an analytical

https://doi.org/10.1017/jfm.2012.547 Published online by Cambridge University Press

solution of the form

$$\hat{v}_0(\eta) = 1 - \eta^2, \quad \frac{\partial \hat{p}_0}{\partial z} = -\frac{8}{Re}, \tag{3.12}$$

$$\hat{v}_1(\eta) = -\eta\left(1 - \eta^2\right)/6, \quad \frac{\partial \hat{p}_1}{\partial z} = 0, \tag{3.13}$$

where (3.12) and (3.13) are identical to the two-term expansion of the reference flow (2.5)–(2.7). Problem (3.10)–(3.11) can be further simplified by assuming that the number of grooves M remains the same while taking the limit $R_1 \to \infty$. This leads to $\alpha = M/R_1 \to 0$, ξ becomes a slow scale and additional simplifications lead to

$$O(1): \quad H_1^2(\eta, \xi)\frac{\partial^2 \hat{v}_0}{\partial \eta^2} = Re\frac{\partial \hat{p}_0}{\partial z}, \tag{3.14a}$$

$$\hat{Q}_0 = \frac{1}{4\pi}\int_0^{2\pi}\int_{-1}^{1} \hat{v}_0(\eta) f(\xi)\, \mathrm{d}\eta\, \mathrm{d}\xi, \tag{3.14b}$$

$$\hat{v}_0(\eta) = 0 \quad \text{at } \eta = \pm 1 \tag{3.14c}$$

$$O(R_1^{-1}): \quad H_1^2(\eta, \xi)\frac{\partial^2 \hat{v}_1}{\partial \eta^2} = Re\frac{\partial \hat{p}_1}{\partial z} - H_1(\eta, \xi)\frac{\partial \hat{v}_0}{\partial \eta}, \tag{3.15a}$$

$$\hat{Q}_1 = \frac{1}{4\pi}\int_0^{2\pi}\int_{-1}^{1} [\hat{v}_0(\eta) F(\eta, \xi) + \hat{v}_1(\eta)] f(\xi)\, \mathrm{d}\eta\, \mathrm{d}\xi, \tag{3.15b}$$

$$\hat{v}_1(\eta) = 0 \quad \text{at } \eta = \pm 1. \tag{3.15c}$$

Problem $O(1)$ is identical to the small-wavenumber approximation of the flow in a straight grooved channel (Mohammadi & Floryan 2011) and problem $O(R_1^{-1})$ combines contributions coming from the curvature (second term on the right-hand side of (3.15*a*)) as well as from the small-wavenumber approximation (left-hand side of (3.15*a*)). Additional contributions from the curvature can be found in the flow rate constraint; $\hat{Q}_1 = 1/3$ in the case of an annulus but $\hat{Q}_1 = 0$ in the case of a straight channel. Equations (3.14) and (3.15) yield an analytical solution of the form

$$\hat{v}_0(\eta) = \left(1 + 3S_{in}^2/8\right)^{-1} f^2(\xi)(1 - \eta^2), \tag{3.16}$$

$$\frac{\partial \hat{p}_0}{\partial z} = -\frac{8}{Re}\left(1 + 3S_{in}^2/8\right)^{-1}, \tag{3.17}$$

$$\begin{aligned}\hat{v}_1(\eta) = {} & f^2(\xi)\left(1 + 3S_{in}^2/8\right)^{-1}(1 - \eta^2)3S_{in}^2\left(1 + 3S_{in}^2/8\right)^{-1}\left(1 + S_{in}^2/16\right)/16 \\ & - f^2(\xi)\left(1 + 3S_{in}^2/8\right)^{-1}(1 - \eta^2)\eta f(\xi)/6,\end{aligned} \tag{3.18}$$

$$\frac{\partial \hat{p}_1}{\partial z} = \frac{-3S_{in}^2}{2Re}\left(1 + 3S_{in}^2/8\right)^{-2}\left(1 + S_{in}^2/16\right). \tag{3.19}$$

The solution for the same grooves but placed on the outer cylinder is given in appendix B.

Figure 2 illustrates variations of the error Er in the evaluation of the pressure gradient using the above approximation. This error is defined as

$$Er = \left|\frac{\partial p}{\partial z} - \frac{\partial \hat{p}_0}{\partial z} - R_1^{-1}\frac{\partial \hat{p}_1}{\partial z}\right| \tag{3.20}$$

where the actual $\partial p/\partial z$ has been determined by solving the complete field equations using a spectrally accurate algorithm to be described in § 4. It can be seen that the

https://doi.org/10.1017/jfm.2012.547 Published online by Cambridge University Press

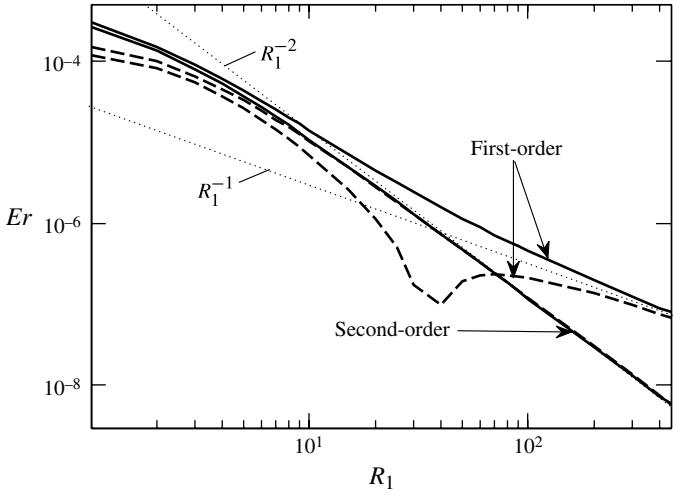


FIGURE 2. Variation of the error of the asymptotic approximation for $R_1 \to \infty$. Solid lines correspond to grooves placed on the inner cylinder (equation (3.7)) with $M = 8$ and $S_{in} = 0.15$ and dashed lines correspond to the same grooves placed on the outer cylinder (see (B 1)).

two-term approximation provides accuracy $O(10^{-7})$ at $R_1 = 10$. Since the first-order approximation is identical to the flow in a straight grooved channel, the difference between this approximation and the full solution provides a means for quantifying the effects of curvature.

4. Numerical solution

This section describes a spectral algorithm used to solve the complete problem (2.1)–(2.4). The algorithm relies on a mapping that transforms the complex geometry into a straight strip suitable for implementation of spectral discretization. An alternative method proposed by Moradi & Floryan (2012) uses the physical domain and enforces boundary conditions on the corrugated boundaries using the concept of immersed boundary conditions. The former method provides better access to configurations with extreme geometries.

4.1. *Discretization of the field equation*

The corrugated annulus in the physical domain (r, θ) is mapped into a smooth annulus in the computational domain (η, ξ) using mapping of the form

$$\xi = \theta, \quad \eta = 2[r - r_{out}(\theta)]\,[r_{out}(\theta) - r_{in}(\theta)]^{-1} + 1. \tag{4.1}$$

The governing equation (2.2) is transformed into

$$W_1(\xi,\eta)\frac{\partial v}{\partial \eta} + W_2(\xi,\eta)\frac{\partial^2 v}{\partial \eta^2} + W_3(\xi,\eta)\frac{\partial^2 v}{\partial \eta \partial \xi} + \frac{\partial^2 v}{\partial \xi^2} = W_4(\xi,\eta) Re \frac{\partial p}{\partial z}, \tag{4.2}$$

where the coefficients

$$\left.\begin{aligned} W_1(\xi,\eta) &= G_3(\eta,\xi) + [A(\xi) + B(\xi)\eta]/B(\xi), \\ W_2(\xi,\eta) &= G_2^2(\eta,\xi) + G_1^2(\eta,\xi)\,[A(\xi) + B(\xi)\eta]^2, \end{aligned}\right\} \tag{4.3a}$$

$$W_3(\xi,\eta) = 2G_2(\eta,\xi), \quad W_4(\xi,\eta) = [A^2(\xi) + 2A(\xi)B(\xi)\eta + B^2(\xi)\eta^2], \tag{4.3b}$$

https://doi.org/10.1017/jfm.2012.547 Published online by Cambridge University Press

contain information about the groove geometry. In the above

$$A(\xi) = 0.5[r_{out}(\xi) + r_{in}(\xi)], \quad B(\xi) = 0.5[r_{out}(\xi) - r_{in}(\xi)], \tag{4.4}$$

$$G_1(\eta, \xi) = B^{-1}(\xi), \quad G_2(\eta, \xi) = -[A_\xi(\xi) + \eta B_\xi(\xi)]B^{-1}(\xi), \tag{4.5a}$$

$$G_3(\eta, \xi) = -[A_{\xi\xi}(\xi) + \eta B_{\xi\xi}(\xi) + 2G_2(\eta, \xi)B_\xi(\xi)]B^{-1}(\xi), \tag{4.5b}$$

and r_{in} and r_{out} are given by (2.1). The boundary conditions take the form

$$v(\xi, 1) = 0, \quad v(\xi, -1) = 0, \tag{4.6}$$

and the flow constraint will be discussed in § 4.2. Solution of (4.2) is periodic in the ξ-direction and thus can be represented in terms of Fourier expansions as

$$v(\xi, \eta) = \sum_{n=-8}^{+8} \Phi^{(n)}(\eta) \mathrm{e}^{\mathrm{i}nM\xi} \approx \sum_{n=-N_M}^{N_M} \Phi^{(n)}(\eta) \mathrm{e}^{\mathrm{i}nM\xi} \tag{4.7}$$

where $\Phi^{(n)} = \Phi^{(-n)*}$. All the known coefficients need to be represented using Fourier expansions, i.e.

$$W_1(\xi, \eta) = \sum_{n=-2N_M}^{2N_M} w_1^{(n)}(\eta) \mathrm{e}^{\mathrm{i}nM\xi}, \quad W_2(\xi, \eta) = \sum_{n=-2N_M}^{2N_M} w_2^{(n)}(\eta) \mathrm{e}^{\mathrm{i}nM\xi}, \tag{4.8a}$$

$$W_3(\xi, \eta) = \sum_{n=-2N_M}^{2N_M} w_3^{(n)}(\eta) \mathrm{e}^{\mathrm{i}nM\xi}, \quad W_4(\xi, \eta) = \sum_{n=-2N_M}^{2N_M} (A_1^{(n)} + 2\eta A_2^{(n)} + \eta^2 A_3^{(n)}) \mathrm{e}^{\mathrm{i}nM\xi}, \tag{4.8b}$$

where $A_1^{(n)}, A_2^{(n)}$ and $A_3^{(n)}$ have the form

$$A_1^{(n)} = \sum_{m=-N_A}^{N_A} A_+^{(m)} A_+^{(n-m)}, \quad A_+^{(n)} = \begin{cases} (1 + 2R_1 + H_{in}^{(0)} + H_{out}^{(0)})/2, & n = 0, \\ (H_{in}^{(n)} + H_{out}^{(n)})/2, & n \neq 0, \end{cases} \tag{4.9a}$$

$$A_2^{(n)} = \sum_{m=-N_A}^{N_A} A_+^{(m)} A_-^{(n-m)}, \quad A_-^{(n)} = \begin{cases} (1 + H_{out}^{(0)} - H_{in}^{(0)})/2, & n = 0, \\ (H_{out}^{(n)} - H_{in}^{(n)})/2, & n \neq 0, \end{cases} \tag{4.9b}$$

$$A_3^{(n)} = \sum_{m=-N_A}^{N_A} A_-^{(m)} A_-^{(n-m)}. \tag{4.9c}$$

Substitution of (4.7)–(4.9) into (4.2) and separation of the Fourier modes leads to

$$\begin{aligned} &-(nM)^2 \Phi^{(n)}(\eta) + \sum_{m=-N_M}^{N_M} \left\{ \left[w_1^{(n-m)}(\eta) + \mathrm{i}mMw_3^{(n-m)}(\eta) \right] \right. \\ &\left. \times \mathrm{D}\Phi^{(m)}(\eta) + w_2^{(n-m)}(\eta) \mathrm{D}^2 \Phi^{(m)}(\eta) \right\} \\ &-(A_1^{(n)} + 2\eta A_2^{(n)} + \eta^2 A_3^{(n)}) Re\, \partial p/\partial z = 0, \end{aligned} \tag{4.10}$$

where $\mathrm{D} = \mathrm{d}/\mathrm{d}\eta$, $-N_M < n < N_M$. The ordinary differential equations (4.10) form a system coupled through the variable coefficients.

The boundary conditions for the modal functions can be written in the form

$$\Phi^{(n)}(1) = 0, \quad \Phi^{(n)}(-1) = 0. \tag{4.11}$$

https://doi.org/10.1017/jfm.2012.547 Published online by Cambridge University Press

Equation (4.10) is discretized using Chebyshev expansions. The unknown $\Phi^{(n)}(\eta)$ and known $w_1^{(n)}(\eta)$, $w_2^{(n)}(\eta)$, $w_3^{(n)}(\eta)$ and $w_4^{(n)}(\eta)$ functions are expressed using Chebyshev expansions of the form

$$\left.\begin{aligned} \Phi^{(n)}(\eta) &= \sum_{k=0}^{N_T} G_k^{(n)} T_k(\eta), \quad w_1^{(n)}(\eta) = \sum_{l=0}^{N_T} G_{l,w1}^{(n)} T_l(\eta), \\ w_2^{(n)}(\eta) &= \sum_{l=0}^{N_T} G_{l,w2}^{(n)} T_l(\eta), \end{aligned}\right\} \tag{4.12a}$$

$$\left.\begin{aligned} w_3^{(n)}(\eta) &= \sum_{l=0}^{N_T} G_{l,w3}^{(n)} T_l(\eta), \\ w_4^{(n)}(\eta) &= (A_1^{(n)} + A_3^{(n)}/2) T_0(\eta) + 2A_2^{(n)} T_1(\eta) + A_3^{(n)} T_2(\eta)/2. \end{aligned}\right\} \tag{4.12b}$$

Substituting (4.12) into (4.10) leads to

$$\begin{aligned} &\sum_{k=0}^{N_T} \Bigg\{ -(nM)^2 G_k^{(n)} T_k(\eta) \\ &\quad + \sum_{m=-N_M}^{N_M} \sum_{l=0}^{N_T} [(G_{l,w1}^{(n-m)} + \mathrm{i}mMG_{l,w3}^{(n-m)}) T_l(\eta) DT_k(\eta) + G_{l,w2}^{(n-m)} T_l(\eta) D^2 T_k(\eta)] G_k^{(m)} \Bigg\} \\ &\quad - Re\ (\partial p/\partial z)\,[(A_1^{(n)} + A_3^{(n)}/2) T_0(\eta) + 2A_2^{(n)} T_1(\eta) + A_3^{(n)} T_2(\eta)/2] = 0. \end{aligned} \tag{4.13}$$

Application of the Galerkin procedure to (4.13) leads to $N_T - 1$ algebraic equations for the unknown coefficients $G_k^{(n)}$ for each Fourier mode of the form

$$\begin{aligned} &\sum_{k=0}^{N_T} \Bigg\{ -(nM)^2 \langle T_j, T_k \rangle G_k^{(n)} \\ &\quad + \sum_{m=-N_M}^{N_M} \sum_{l=0}^{N_T} ([G_{l,w1}^{(n-m)} + \mathrm{i}mMG_{l,w3}^{(n-m)}] \langle T_j, T_l DT_k \rangle + G_{l,w2}^{(n-m)} \langle T_j, T_l D^2 T_k \rangle) G_k^{(m)} \Bigg\} \\ &\quad - Re\,(\partial p/\partial z)[(A_1^{(n)} + A_3^{(n)}/2) \langle T_j, T_0 \rangle + 2A_2^{(n)} \langle T_j, T_1 \rangle + A_3^{(n)} \langle T_j, T_2 \rangle/2] = 0. \end{aligned} \tag{4.14}$$

Substitution of (4.12) into (4.11) leads to boundary conditions expressed in terms of coefficients of Chebyshev expansions of the form

$$\sum_{k=0}^{N_T} G_k^{(n)} = 0, \quad \sum_{k=0}^{N_T} (-1)^k G_k^{(n)} = 0. \tag{4.15}$$

These conditions are enforced by replacing equations of type (4.14) for the two largest coefficients of Chebyshev expansions with (4.15), i.e. the tau method.

4.2. *Flow constraint*

The pressure gradient $\partial p/\partial z$ needs to be determined as a part of the solution process and the fixed flow rate constraint provides the required closing condition. Evaluation of the fixed flow rate constraint begins with expressing the axial velocity in terms of

https://doi.org/10.1017/jfm.2012.547 Published online by Cambridge University Press

the discretized variables, i.e.

$$\frac{Q_{ref}}{M} = \int_0^{2\pi/M} \int_{\eta=-1}^{\eta=1} \left\{ \left[A(\xi)B(\xi) + B^2(\xi)\eta\right] \sum_{n=-N_M}^{N_M} \sum_{k=0}^{N_T} G_k^{(n)} T_k(\eta) \mathrm{e}^{\mathrm{i}nM\xi} \right\} \mathrm{d}\eta\, \mathrm{d}\xi. \quad (4.16)$$

Substituting (4.9) into (4.16), expressing η in terms of Chebyshev expansion and evaluating the inner integral leads to

$$\frac{Q_{ref}}{M} = 0.5 \sum_{n=-2N_M}^{2N_M} \sum_{m=-N_M}^{N_M} \sum_{k=0}^{N_T} G_k^{(m)} \left[2\hat{I}_k A_2^{(n-m)} + (\hat{I}_{k+1} + \hat{I}_{|k-1|}) A_3^{(n-m)}\right] \times \int_0^{2\pi/M} \mathrm{e}^{\mathrm{i}nM\xi}\, \mathrm{d}\xi, \quad (4.17)$$

where

$$\left.\begin{aligned} &\hat{I}_0 = 2, \quad \hat{I}_1 = 0, \\ &\hat{I}_k = \int_{\eta=-1}^{\eta=1} T_k(\eta)\, \mathrm{d}\eta = \frac{1}{2}\left[\frac{1-(-1)^{k+1}}{k+1} - \frac{1-(-1)^{k-1}}{k-1}\right], \quad k \geqslant 2. \end{aligned}\right\} \quad (4.18)$$

The integrals in (4.17) have the property

$$\int_0^{2\pi/M} \mathrm{e}^{\mathrm{i}nM\xi}\, \mathrm{d}\xi = \begin{cases} 2\pi/M, & n = 0, \\ 0, & n \neq 0, \end{cases} \quad (4.19)$$

which leads to the form of the constant volume flow rate constraint suitable for computations, i.e.

$$\sum_{m=-N_M}^{N_M} \sum_{k=0}^{N_T} G_k^{(m)} \left[2\hat{I}_k A_2^{(-m)} + (\hat{I}_{k+1} + \hat{I}_{|k-1|}) A_3^{(-m)}\right] = \frac{Q_{ref}}{\pi}. \quad (4.20)$$

4.3. *Evaluation of surface stress*

This section describes the procedure used for the evaluation of the shear stresses acting on the inner cylinder. A similar procedure can be easily developed for the outer cylinder. The non-zero elements of the stress tensor are

$$\tau_{rz} = \frac{-1}{Re}\frac{\partial v}{\partial r}, \quad \tau_{\theta z} = \frac{-1}{rRe}\frac{\partial v}{\partial \theta}. \quad (4.21)$$

The component of the shear stress acting on the wall in the z-direction has the form

$$\mathrm{d}F_{total,z} = n_\theta \tau_{\theta z} + n_r \tau_{rz} \quad (4.22)$$

where $\boldsymbol{n} = (n_\theta, n_r, n_z)$ is the normal unit vector pointing outward, $n_r = -N^{-1}$, $n_\theta = (r_{in}N)^{-1}\, \mathrm{d}r_{in}/\mathrm{d}\theta$, $n_z = 0$, $N = [1 + r_{in}^{-2}\, (\mathrm{d}r_{in}/\mathrm{d}\theta)^2]^{1/2}$. The total force acting on the wall can be computed as

$$F_{total,z} = \int_{S_{in}} \mathrm{d}F_{total,z}\, \mathrm{d}S_{in} \quad (4.23)$$

where $\mathrm{d}S_{in} = r_{in}N\, \mathrm{d}\theta$. The components of the stress tensor expressed in terms of the discretized variables are given in appendix C.

https://doi.org/10.1017/jfm.2012.547 Published online by Cambridge University Press

5. Groove-induced flow modifications

A constant pressure gradient needs to be applied along the annulus in order to produce a desired flow rate. We shall refer to this pressure gradient as a pressure loss. The introduction of grooves may increase/decrease this pressure loss depending on the groove geometry and the flow conditions. The main objective of this analysis is the determination of the role played by all these factors in the creation of the pressure loss and identification of the forms of the grooves that may reduce drag. The additional pressure gradient required to maintain the same flow rate in the grooved annulus as in the smooth reference (i.e. with the same flow cross-sectional area) annulus is adopted as the principal measure of the groove effects.

The pressure gradient is expressed, for convenience, in terms of a friction factor

$$f = -2\frac{\partial p}{\partial z} = -2\frac{\partial p_0}{\partial z} - 2\frac{\partial p_1}{\partial z} = f_0 + f_1, \tag{5.1}$$

where f denotes the total friction factor, $f_0 = 8/(k_1 Re)$ denotes the friction factor for the smooth annulus (we shall refer to it as the reference friction factor), f_1 stands for the modification friction factor associated with the presence of the grooves and f_1/f_0 will be referred to as the normalized modification friction factor.

There is an uncountable number of possible groove shapes and positions. In order to provide a systematic presentation, this discussion begins with the demonstration that the complete effect can be decomposed into: (i) the effect due to a change in the average position of each cylinder (i.e. change of the flow cross-sectional area); and (ii) the effect due to spatial flow modulations created by the grooves. The change in the cross-sectional area is always represented as change in the radius of the reference circular cylinder as the focus of this analysis is on circular annuli fitted with grooves.

5.1. *Effect of the average position of the bounding cylinders*

Changing the cross-sectional flow area has a very strong effect on the pressure losses and is unrelated to any flow modulations created by the grooves. This change can be introduced intentionally through the direct specification of the coefficients of the zeroth modes in (2.1), i.e. $H_{in}^{(0)}$ and $H_{out}^{(0)}$. Specification of the remaining coefficients in (2.1) produces inadvertent change in the cross-sectional area due to the radial effects. In order to provide a correct physical interpretation of the results, this change needs to be properly compensated for so that one can separate the pressure losses associated with the flow modulations from those associated with the change in the flow cross-sectional area. Evaluation of the required correction factor $R_{in,c}$ for the inner cylinder is explained below.

The cross-sectional area of the reference (smooth) cylinder is $A_{smooth} = \pi R_1^2$. The cross-sectional area of the grooved cylinder is expressed as

$$A_{grooved} = \pi(R_1 + R_{in,c})^2 + 2\pi(R_1 + R_{in,c})H_{in}^{(0)} + \pi\sum_{m=0}^{N_A} |H_{in}^{(m)}|^2, \tag{5.2}$$

where $R_{in,c}$ denotes the correction that must be applied in order to have the same cross-sectional areas for the smooth and the grooved cylinders. Since $A_{smooth} = A_{grooved}$, the correction factor becomes

$$R_{in,c} = \sqrt{(R_1 + H_{in}^{(0)})^2 - \left(2R_1 H_{in}^{(0)} + \sum_{m=1}^{N_A} |H_{in}^{(m)}|^2\right)} - (R_1 + H_{in}^{(0)}). \tag{5.3}$$

https://doi.org/10.1017/jfm.2012.547 Published online by Cambridge University Press

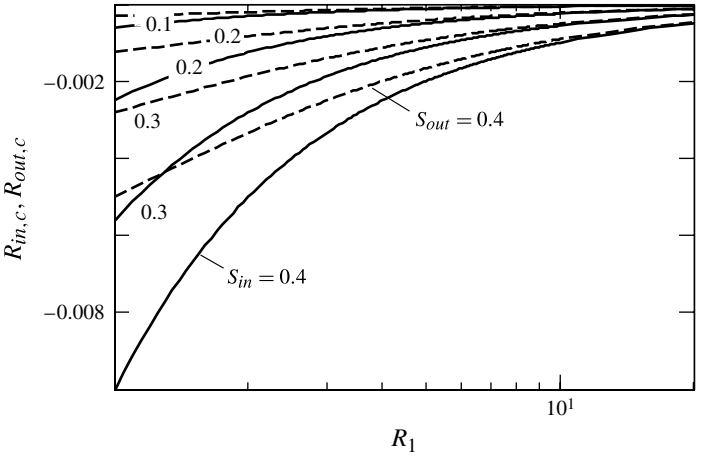


FIGURE 3. Variations of the geometric correction factors $R_{in,c}$ and $R_{out,c}$ as functions of R_1 for the groove geometry described by (5.4) with $S_{ave,in} = S_{ave,out} = \varphi = 0$ with the same grooves placed either on the inner cylinder (solid lines, $S_{in} = 0.1$, $S_{out} = 0$) or on the outer cylinder (dashed lines, $S_{in} = 0$, $S_{out} = 0.1$).

A similar procedure can be used to evaluate the correction factor $R_{out,c}$ for the outer cylinder. Variations of $R_{in,c}$ and $R_{out,c}$ as functions of R_1 are illustrated in figure 3 for the groove geometry specified as

$$\left.\begin{aligned} r_{in}(\theta) &= R_1 + S_{ave,in} + 0.5S_{in}\cos(M\theta), \\ r_{out}(\theta) &= 1 + R_1 + S_{ave,out} + 0.5S_{out}\cos\left[M(\theta+\varphi)\right], \end{aligned}\right\} \tag{5.4}$$

with $S_{ave,in} = S_{ave,out} = \varphi = 0$. It can be observed that both $R_{in,c}$ and $R_{out,c}$ become negligible when $R_1 > 10$. The same grooves produce a larger correction when placed on the inner rather than on the outer cylinder.

Flow modulation effects can be separated from the effects associated with the change of the average position of the wall by writing (2.1) as

$$r_{in}(\theta) = \left\{ R_1 + R_{in,c} + \sum_{n=-N_A, n\neq 0}^{N_A} H_{in}^{(n)} \mathrm{e}^{\mathrm{i}nM\theta} \right\} - R_{in,c} + H_{in}^{(0)}, \tag{5.5a}$$

$$r_{out}(\theta) = \left\{ R_1 + R_{out,c} + \sum_{n=-N_A, n\neq 0}^{N_A} H_{out}^{(n)} \mathrm{e}^{\mathrm{i}nM\theta} \right\} - R_{out,c} + H_{out}^{(0)}, \tag{5.5b}$$

where the curly brackets capture the effects of spatial modulations and the remaining terms account for the change in the flow cross-sectional area.

In order to assess the effects of changes in the average position of the cylinders, consider an annulus with geometry given by (5.4) with $S_{in} = S_{out} = \varphi = 0$. To maintain the same flow rate as in the reference annulus, the following pressure gradient has to

https://doi.org/10.1017/jfm.2012.547 Published online by Cambridge University Press

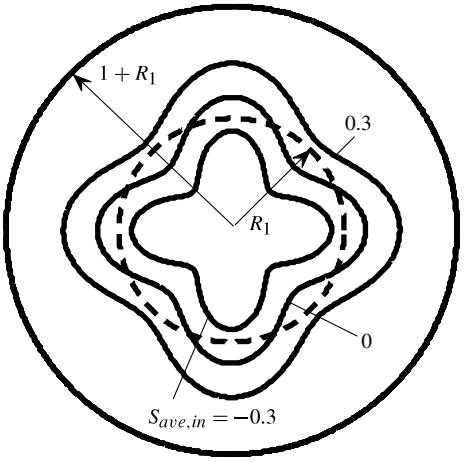


FIGURE 4. Sketch of the test configuration used to demonstrate the effect of the average position $S_{ave,in}$ of the grooves. Four grooves ($M=4$) with the shape defined by (5.4) with $S_{in}=0.3$, $S_{out}=0$, $S_{ave,out}=0$ are placed at three different average locations: Case A $S_{ave,in}=0.3$; Case B $S_{ave,in}=0$; Case C $S_{ave,in}=-0.3$. See text for details.

be imposed:

$$\frac{\mathrm{d}p}{\mathrm{d}z}=-4\,(Rek_1)^{-1}\left[(R_1^2-k_2/2)(1+2R_1)\right.$$
$$\left.+k_2\,(1+R_1)^2\ln\left((1+R_1)R_1^{-1}\right)-(1+R_1)^4\,/2+R_1^4/2\right]$$
$$\times\left\{-(e_1^4-e_2^4)/2+d_1e_1^2\ln e_1-d_1e_2^2\ln e_2+(d_2-d_1/2)(e_1^2-e_2^2)\right\}^{-1},\quad(5.6)$$

where

$$d_1=\frac{e_1^2-e_2^2}{\ln(e_1/e_2)},\quad(5.7)$$

$$d_2=\frac{e_2^2\ln e_1-e_1^2\ln e_2}{\ln(e_1/e_2)},\quad(5.8)$$

and $e_1=1+R_1+S_{out,ave}$, $e_2=R_1+S_{in,ave}$. The change in the pressure gradient due the change in the average wall position can be easily determined by comparing (5.6) and (2.6).

Now consider the annulus sketched in figure 4 with the geometry described by (5.4) with $S_{out}=0$, $S_{ave,out}=0$. Variations of the additional pressure loss as a function of the amplitude S_{in} are depicted in figure 5 for three different average positions $S_{ave,in}$. Cases A, B, C correspond to $S_{ave,in}=0.05, 0, -0.05$, respectively. Equation (5.6) gives the additional friction factors for the limit $S_{in}=0$ (smooth annulus) as $f_1\,Re=2.3442, 0, -1.9355$ for cases A, B and C, respectively.

Friction factors for the corrugated annuli have been determined numerically using the methodology described in § 4. The results displayed in figure 5 show that changes of the friction factor as a function of the groove amplitude are identical in all cases when the shift defined by (5.6) is accounted for. This demonstrates that the total modification friction factors can be represented as a superposition of the effects associated with the change in the mean position of the cylinders and the effects of the shape-induced spatial flow modulation. The former effects can be determined analytically, e.g. (5.6).

https://doi.org/10.1017/jfm.2012.547 Published online by Cambridge University Press

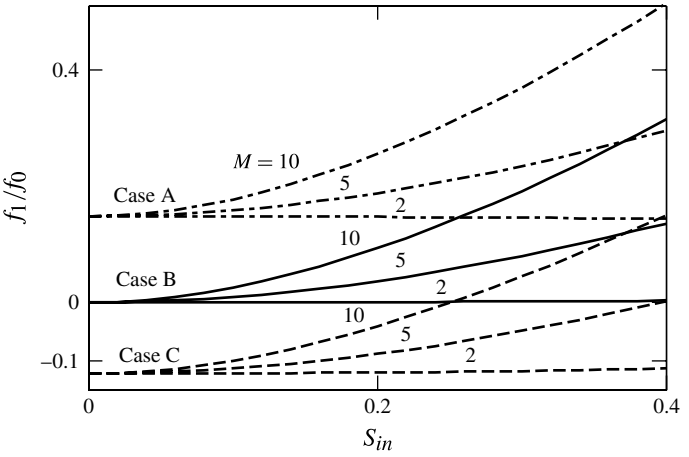


FIGURE 5. Variation of the normalized modification friction factor f/f_0 as a function of groove amplitude S_{in} for $R_1 = 1$ and selected values of M. Grooves are placed on the inner cylinder with their geometry defined by (5.4) with $S_{ave,out} = S_{out} = 0$ and $S_{ave,in} = 0.05, 0, -0.05$ in cases A–C, respectively.

5.2. *Reduced-order representation of groove shape*

We shall now focus attention on the assessment of flow modulations created by the grooves. There is an uncountable number of possible shapes and general conclusions may not be possible as we cannot check all possible shapes. In order to overcome this difficulty, the 'primitive' form of the specification of groove shape, e.g. the left side of (2.1), is replaced with its projection onto a Fourier space, e.g. the right-hand side of (2.1), producing a reduced-order geometry model. It has been shown by Floryan (2007) that use of the leading Fourier mode in the shape specification is sufficient for prediction of the critical stability conditions with an accuracy acceptable for most applications. The same conclusion has been reached by Mohammadi & Floryan (2011) who studied pressure losses in grooved channels. We shall now determine if the same procedure provides acceptable accuracy for prediction of pressure losses in grooved annuli and determine the level of accuracy obtained by replacing the actual groove with the first term of its representation in the Fourier space.

Figure 6 depicts four shapes selected for this study, i.e. rectangular, trapezoidal, triangular and rectified. Tests have been carried out for cylinders with the same radius R_1 equipped with M identical grooves. The results displayed in figure 7 demonstrate that the modification friction factor converges very rapidly to the actual value as the number of Fourier modes N_A used for representation of groove geometry increases (values computed with $N_A = 100$ were taken as representing the actual values). The use of just one Fourier mode for the geometry representation leads to an under-prediction of losses by $\sim$10 %, which is most likely to be acceptable in the majority of applications. The convergence is noticeably slower in the case of the rectangular groove where the Gibb's phenomenon affects the convergence of the Fourier series for the shape representation. The reader should note that the one-Fourier-mode model is able to capture the properties of grooves that have the same maximum depth and height, but has to be supplemented by additional Fourier modes when depth and height are not the same. This issue will be discussed in § 6.

https://doi.org/10.1017/jfm.2012.547 Published online by Cambridge University Press

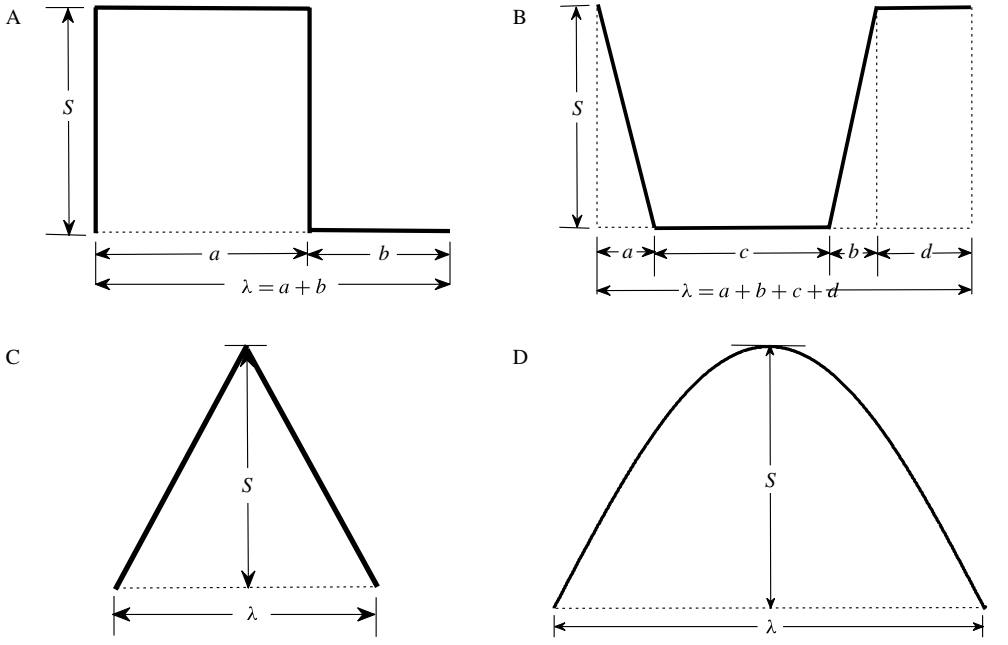


FIGURE 6. Shapes of the grooves used in this study: A rectangular; B trapezoidal; C triangular; D rectified ($|\sin M\theta|$). λ denotes the length of one groove segment.

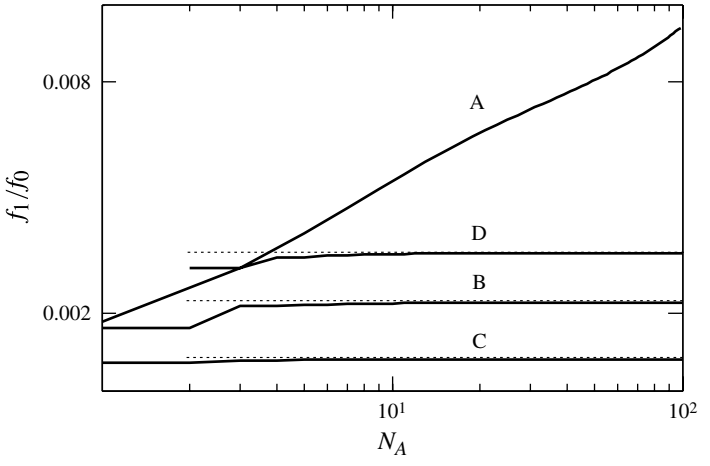


FIGURE 7. Variation of the normalized modification friction factor f_1/f_0 as a function of the number of Fourier modes N_A used to describe the groove geometry. Four grooves ($M = 4$) with shapes A–D described in figure 6 and the same amplitude $S_{in} = 0.1$ are placed on the inner cylinder with average radius $R_1 = 1$ in such a way that mode zero of their Fourier expansion is zero. For groove A: $a = b = \pi/M$; for groove B: $a = b = \pi/3M$, $c = 2\pi/3M$.

5.3. *Effect of the dominant geometric parameters*

The dominant effects created by flow modulations can be captured by replacing the actual groove geometry with the leading Fourier mode from its Fourier representation,

https://doi.org/10.1017/jfm.2012.547 Published online by Cambridge University Press

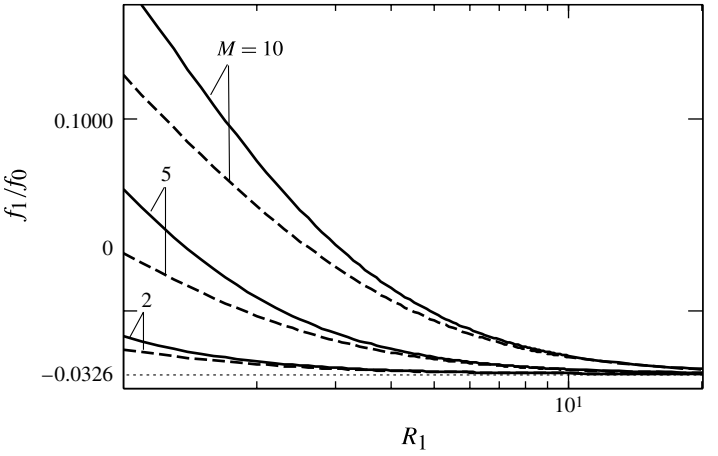


FIGURE 8. Variation of the normalized modification friction factor f_1/f_0 as a function of R_1 for the geometry described by (5.4) with $S_{ave,out} = S_{ave,in} = 0$ and $M = 2, 5$ and 10. Solid (dashed) lines correspond to the same grooves placed only on the inner (outer) cylinder with $S_{in} = 0.3$, $S_{out} = 0$ ($S_{in} = 0$, $S_{out} = 0.3$).

as shown in § 5.2. The reference geometry is therefore given by (5.4) with $S_{ave,in} = S_{ave,out} = 0$, with S_{in}, S_{out}, φ, M and R_1 being the main parameters. Evaluation of the friction factor for any geometry can be reduced to the determination of its leading Fourier mode and use of data to be presented later in this Section. More complete reference tables can be easily created. The accuracy of this procedure can be improved by taking advantage of the fact that the use of the leading Fourier mode always under-predicts pressure losses (as discussed in § 5.2). The reader should note that the number of Fourier modes required for an accurate description of the flow field is larger than the number of Fourier modes required for description of the geometry; this number needs to be established through numerical experiments.

We shall begin discussion with an annulus fitted with grooves placed on only one of the cylinders. Figure 8 demonstrates that the most rapid changes of pressure gradient due to increase of R_1 occur for small values of R_1; the rate of change rapidly decreases and the pressure gradient approaches the asymptotic limit corresponding to a two-dimensional grooved channel. An increase in the number of grooves along the circumference increases losses. Grooves placed on the inner cylinder produce a greater change in the pressure gradient than the same grooves placed on the outer cylinder. It is remarkable that the presence of grooves leads to the reduction of the pressure loss (negative f_1) for large enough R_1. Since an increase in the number of grooves (larger M) increases the pressure loss, larger R_1 is required to effect drag reduction under such conditions. Figure 9 illustrates variations of the modification friction factor as a function of the amplitudes S_{in}, S_{out} and the radius R_1 for annuli equipped with different numbers of grooves placed either on the inner or on the outer cylinder. An increase of both S_{in} and S_{out} increases losses for small R_1 but decreases losses for larger R_1; the boundary between the drag reduction and the drag increase marginally depends on the magnitudes of S_{in} and S_{out} and shifts towards larger values of R_1 when M increases. There is only drag reduction when the annulus is equipped with a small number of grooves, e.g. figure 9(*a*) for $M = 2$. An increase of M always increases drag. This can

https://doi.org/10.1017/jfm.2012.547 Published online by Cambridge University Press

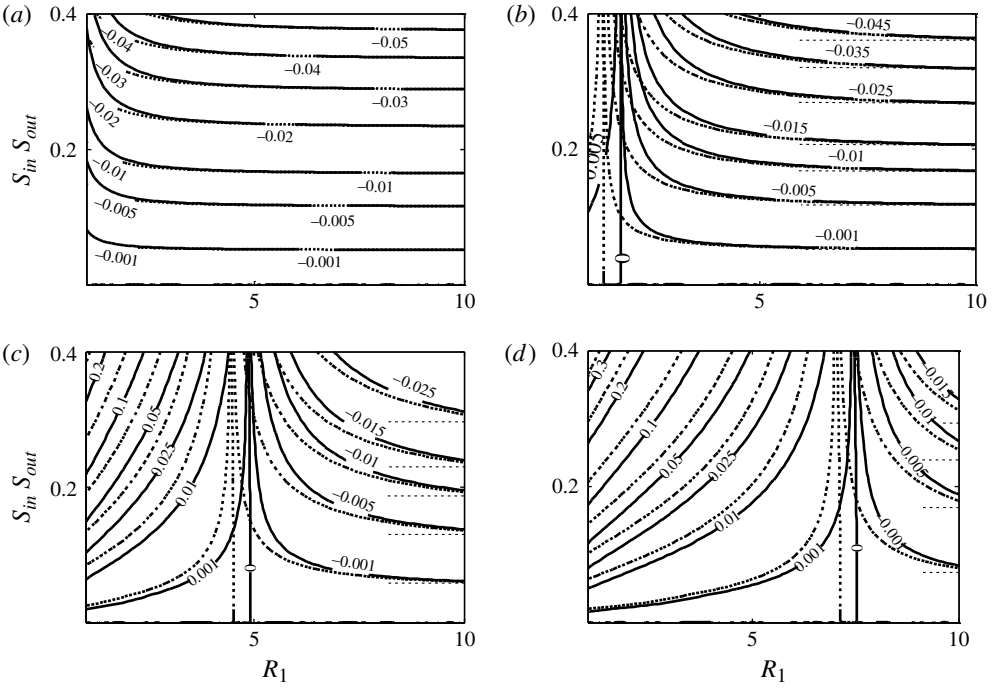


FIGURE 9. Variation of the normalized modification friction factor f_1/f_0 as a function of the groove amplitudes S_{in} and S_{out} and the radius of the inner cylinder R_1 for the geometry described by (5.4) with $S_{ave,out} = S_{ave,in} = 0$. Results for $M = 2, 4, 10, 15$ grooves are displayed in (*a–d*) respectively. Solid (dashed) lines correspond to grooves placed only on the inner (outer) cylinder.

be counteracted by an increase of R_1 which eventually changes this trend and leads to drag reduction regardless of the value of M.

The results displayed in figure 10 demonstrate that the conditions leading to the drag reduction correlate well with the groove wavenumber $\alpha = M/R_1$. Drag reduction is observed for M/R_1 smaller than the critical value α_c, where α_c does not depend on Re as a change of Re cannot affect the sign of the pressure loss (see (2.2)). The magnitude of the drag reduction increases proportionally to S^2 with S denoting the amplitude of the corrugation; $S = S_{in}$ when the corrugation is placed on the inner cylinder and $S = S_{out}$ when the roughness is placed on the outer cylinder. The opposite occurs when M/R_1 is larger than α_c. The value of α_c depends on the number of grooves and approaches $\alpha_c \approx 1.92$ when M increases, as documented in figure 11. The friction factor does not depend on R_1 when the radius becomes large enough (see figure 9) as the effects of curvature become negligible and the flow behaviour is very similar to flow in a two-dimensional grooved channel (see § 3). The friction factor also loses its dependence on the groove wavenumber when M/R_1 becomes small enough (see figure 10) and rapidly approaches the limiting value given by the small-wavenumber approximation of flow in a two-dimensional grooved channel (see § 3).

Figure 12 displays variations of the modification friction factor as a function of the phase difference φ between the grooves on both cylinders and the cylinder radius R_1. It can be seen that the largest drag corresponds to $\varphi = 0$, i.e. grooves are in

https://doi.org/10.1017/jfm.2012.547 Published online by Cambridge University Press

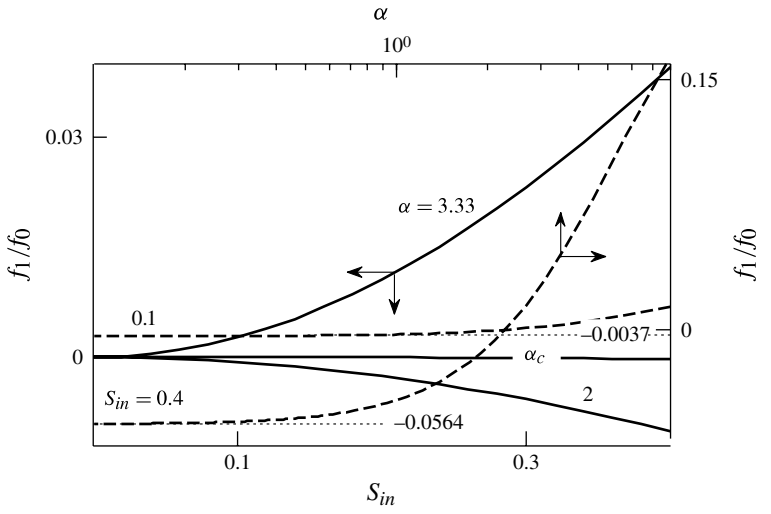


FIGURE 10. Variation of the normalized modification friction factor f_1/f_0 induced by the grooves placed on the inner cylinder with the shape defined by (5.4) with $S_{ave,out} = S_{ave,in} = S_{out} = 0$ and $M = 4$, as a function of the amplitude S_{in} (solid lines and left-hand axis) and as a function of the wavenumber $\alpha = M/R_1$ (dashed lines and right-hand axis).

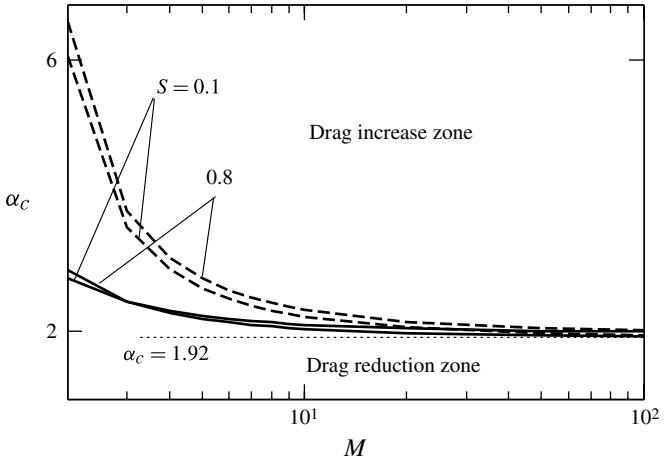


FIGURE 11. Variation of the critical groove wavenumber α_c as a function of the number of grooves M for an annulus with geometry described by (5.4) with $S_{ave,out} = S_{ave,in} = 0$. Solid (dashed) line corresponds to the grooves placed only on the inner (outer) cylinder with $S_{in} = 0.1$ and 0.8, $S_{out} = 0$ ($S_{in} = 0$, $S_{out} = 0.1$ and 0.8).

phase and the annular opening has a wavy pattern in the circumferential direction, and the smallest drag corresponds to grooves being out of phase ($\varphi = \pi/M$) and the converging–diverging pattern. Drag reduction can be induced for a sufficiently large R_1 for grooves with all possible phase differences, but this reduction is the largest and occurs for the smallest R_1 when grooves are out of phase.

https://doi.org/10.1017/jfm.2012.547 Published online by Cambridge University Press

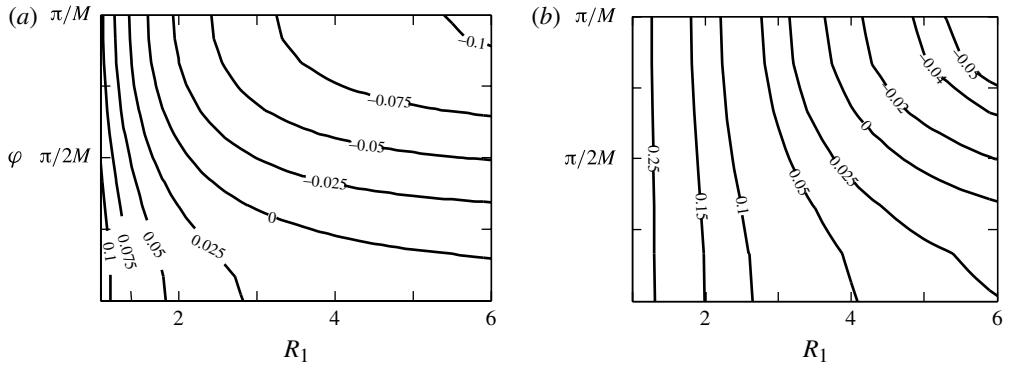


FIGURE 12. Variation of the normalized modification friction factor f_1/f_0 as a function of the groove phase difference φ and the radius of the inner cylinder R_1 for the grooves described by (5.4) with $S_{in} = S_{out} = 0.3$ and $S_{ave,out} = S_{ave,in} = 0$. (*a*) Results for $M = 5$ grooves and (*b*) 10 grooves.

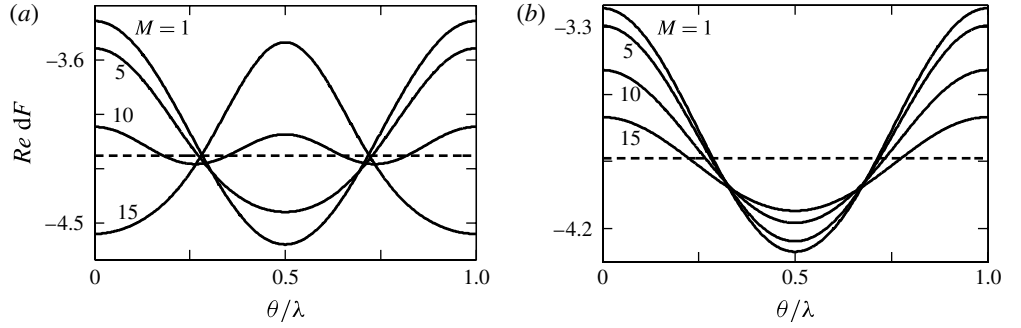


FIGURE 13. Distribution of the axial component of shear stress acting on the fluid at the inner (*a*) and outer (*b*) cylinders for grooves with the geometry defined by (5.4) with $S_{in} = 0.3$, $S_{out} = 0$, $R_1 = 5$ and $S_{ave,out} = S_{ave,in} = 0$. Dashed lines provide reference values for the smooth cylinders.

5.4. *Drag reduction mechanism*

It is of interest to identify the processes that lead to the observed drag reduction. The distribution of the shear stress acting on the fluid displayed in figure 13 shows a remarkable difference in the drag-reducing and the drag-increasing cases. In the former case the magnitude of the shear at the grooved cylinder (inner cylinder in the case shown in figure 13) reaches a minimum at locations corresponding to the minima of the annulus opening and reaches a maximum in locations corresponding to the maxima of the annulus opening. In the latter case, the distribution is reversed with the shear stress maxima occurring at locations corresponding to the minima of the annulus opening. The distribution of the shear stress at the outer (smooth) cylinder remains qualitatively the same under the drag-reducing and the drag-increasing conditions, with the maxima occurring at the locations corresponding to the maxima of the annulus opening.

The difference between the minimum and the maximum of the shear stress (amplitude of the shear stress variations) decreases as M increases in the drag-reducing

https://doi.org/10.1017/jfm.2012.547 Published online by Cambridge University Press

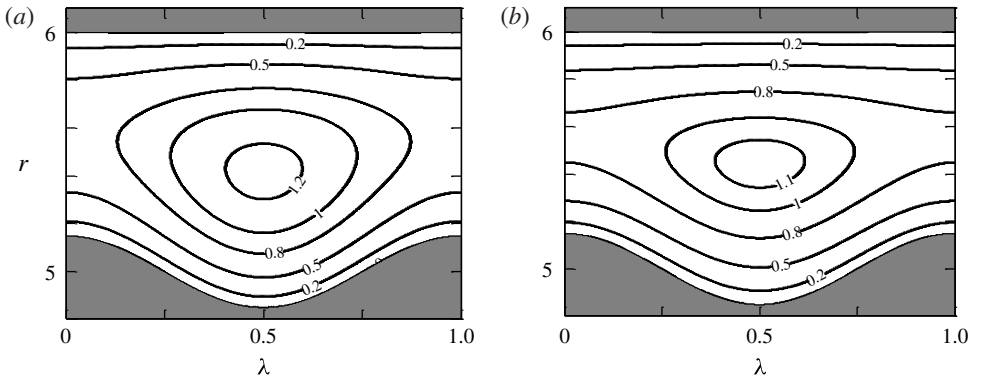


FIGURE 14. Distribution of the axial velocity component in an annulus with the geometry defined by (5.4) with $S_{in} = 0.3$, $R_1 = 5$, $S_{ave,out} = S_{ave,in} = S_{out} = 0$ and $M = 5$ (*a*) and $M = 15$ (*b*).

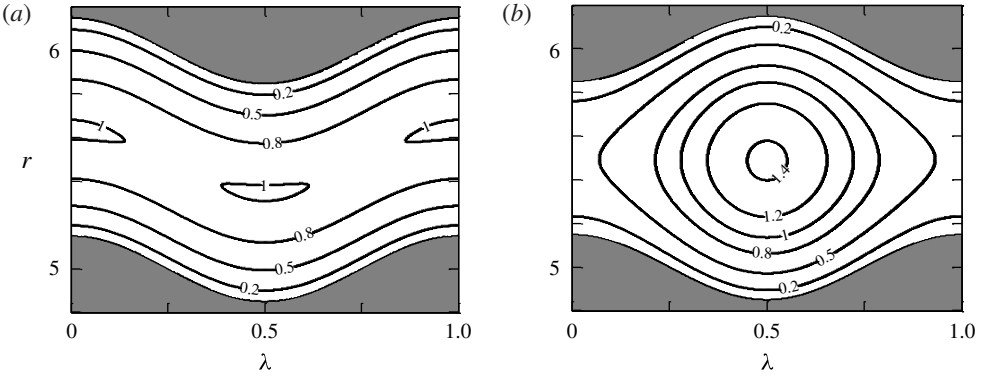


FIGURE 15. Distribution of the axial velocity component in an annulus with the geometry defined by (5.4) with $S_{in} = S_{out} = 0.3$, $R_1 = 5$, $S_{ave,out} = S_{ave,in} = 0$, $M = 5$ and $\varphi = 0$ (*a*) and $\varphi = \pi$ (*b*).

configuration. This amplitude passes through the value for a smooth annulus for M corresponding to its critical value, and starts to increase again with further increase of M (see figure 13*a*).

Figure 14 displays constant-velocity lines. It can be seen that presence of grooves leads to a re-arrangement of the bulk flow, with stream tubes of high-velocity fluid forming in the area of the largest annulus opening under drag-reducing conditions (figure 14*a*). Changes in the groove geometry leading to a drag increase result in the reduction of the high-velocity stream tubes; this is demonstrated in figure 14(*b*) through the increase of M while keeping the remaining parameters the same. A similar reduction of these stream tubes can be observed when the phase difference between the grooves on both walls decreases to zero (see figure 15) which leads to a drag increase, as discussed in § 5.4. It can be concluded that it is the re-arrangement of the bulk flow that is responsible for the drag reduction in spite of an increase of the wetted surface area.

https://doi.org/10.1017/jfm.2012.547 Published online by Cambridge University Press

6. Groove optimization for drag reduction

It has been shown in §§ 5.3 and 5.4 that the presence of grooves may lead to a reduction of pressure losses. This section is focused on finding the groove shape that leads to the largest possible drag reduction in the case of an annulus with radius R_1 fitted with M grooves. It has been argued in § 5.2 that a good approximation of the pressure loss can be found by replacing the actual grooves with the first mode of their Fourier representation (reduced-order model). The optimization requires access to a wider range of information about the geometry and thus one needs to include higher Fourier modes.

It is simpler to discuss the optimization by describing the groove geometry in terms of real variables, i.e.

$$r_{in}(\theta) = R_1 + A_{1,in}\cos(M\theta) + A_{2,in}\cos(2M\theta + \varphi_{2,in}) + \cdots + A_{n,in}\cos(nM\theta + \varphi_{n,in}), \tag{6.1a}$$

$$r_{out}(\theta) = 1 + R_1 + A_{1,out}\cos(M\theta + \varphi_{1,out}) + A_{2,out}\cos(2M\theta + \varphi_{2,out}) + \cdots + A_{m,out}\cos(mM\theta + \varphi_{m,out}). \tag{6.1b}$$

The optimization problem involves finding the minimum of

$$f_1 Re = F(A_{1,in}, \ldots, A_{n,in}, \varphi_{2,in}, \ldots, \varphi_{n,in}, A_{1,out}, \ldots, A_{m,out}, \varphi_{1,out}, \ldots, \varphi_{m,out}) \tag{6.2}$$

subject to suitable constraints. It can be shown, on the basis of symmetry arguments as well as direct evaluations of pressure losses, e.g. figure 12, that the maximum drag reduction corresponds to either zero or π phase shift. Thus the optimization is reduced to finding the minimum of

$$f_1 Re = F(A_{1,in}, \ldots, A_{n,in}, A_{1,out}, \ldots, A_{m,out}). \tag{6.3}$$

The optimization is focused on the effects of flow modulations and thus the flow cross-sectional area has to be kept constant during the search process. This leads to a nonlinear constrained optimization problem which is solved using the trust-region-reflective optimization algorithm (Coleman & Li 1994, 1996). Details related to the actual implementation of this algorithm are discussed in the next section.

The optimization requires specification of the range of acceptable geometries. In the present analysis, one needs to specify the constraints imposed on the maximum permissible depths and heights of the grooves measured from the reference cylinders. The depth and the height can be treated as unknowns to be determined by the optimization process. If this is the case and M is in the region of drag increase (see figure 11), the optimization always results in the removal of the grooves. In the case of M corresponding to drag reduction, the results of the optimization depend on the type of the imposed constraint. The following discussion addresses this particular issue.

6.1. *Equal-depth grooves*

As the first case, consider grooves placed only on the inner cylinder. It is assumed that the maximum depth and the maximum height of these grooves are the same. We shall refer to such geometry as the equal-depth grooves. The relevant constraints can be expressed as

$$\max_\theta |r_{in}(\theta)| = R_1 + S_{in,o}, \quad \min_\theta |r_{in}(\theta)| = R_1 - S_{in,i}, \quad S_{in,i} = S_{in,o}, \tag{6.4a–c}$$

$$\max_\theta |r_{out}(\theta)| = \min_\theta |r_{out}(\theta)| = 1 + R_1, \tag{6.4d}$$

where $S_{in,i}$ and $S_{in,o}$ stand for the height and the depth of the groove, respectively. Constraints (6.4) need to be supplemented by a constraint expressing conservation of

https://doi.org/10.1017/jfm.2012.547 Published online by Cambridge University Press

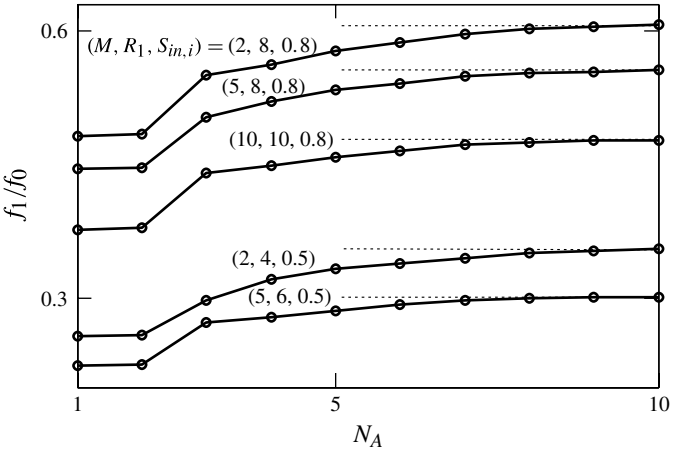


FIGURE 16. Variation of the normalized modification friction factor f_1/f_0 as a function of the number of Fourier modes used for description of the optimal shape of the equal-depth grooves placed on the inner cylinder.

the flow cross-sectional area. One may pose a constraint where the depth and the height of the groove cannot exceed a certain threshold, i.e.

$$\max_\theta |r_{in}(\theta)| \leqslant R_1 + S_{in,o}, \quad \min_\theta |r_{in}(\theta)| \leqslant R_1 - S_{in,i}, \quad S_{in,i} = S_{in,o}, \quad (6.5a\text{–}c)$$

$$\max_\theta |r_{out}(\theta)| = \min_\theta |r_{out}(\theta)| = 1 + R_1. \quad (6.5d)$$

Such constraints need not be considered as the minimum drag always correspond to the maximum permitted height and depth.

The shapes of the optimal grooves are expressed by Fourier expansions with an unknown number of terms. The results displayed in figure 16 for typical conditions of interest demonstrate that these expansions are fairly rapidly convergent. Use of just three Fourier modes allows approximation of the optimal shape with less than a 10 % error for the pressure loss. The error can be reduced by using additional modes (see figure 16). These results, as well as those from many other similar tests (not reported), lead to a conclusion that the reduced-order models based on 3–4 Fourier modes can capture the optimal shapes with an accuracy that is sufficient for most applications.

The insensitivity of the pressure loss to details of the geometry expressed by higher Fourier modes should not be surprising as the action of viscosity is expected to smooth out such details. This, however, creates computational problems as gradients of the cost function with respect to higher Fourier modes that need to be computed by the optimizer become very small. These gradients are determined using low-order finite-difference quotients. Use of strict convergence criteria is able, however, to overcome these difficulties but at a considerable computational cost. Once the convergence of a Fourier series has been established, as illustrated in figure 16, the actual computations can be carried out using fewer Fourier modes and less-strict convergence criteria. All of the results presented in this paper have been obtained with the convergence criteria set at 10^{-6} and the use of 10 Fourier modes depending on the form of the optimal grooves.

We shall now discuss the form of the optimal grooves. Evolution of the optimal shape when the inner cylinder is fitted with $M = 2, 10$ grooves with amplitudes

https://doi.org/10.1017/jfm.2012.547 Published online by Cambridge University Press

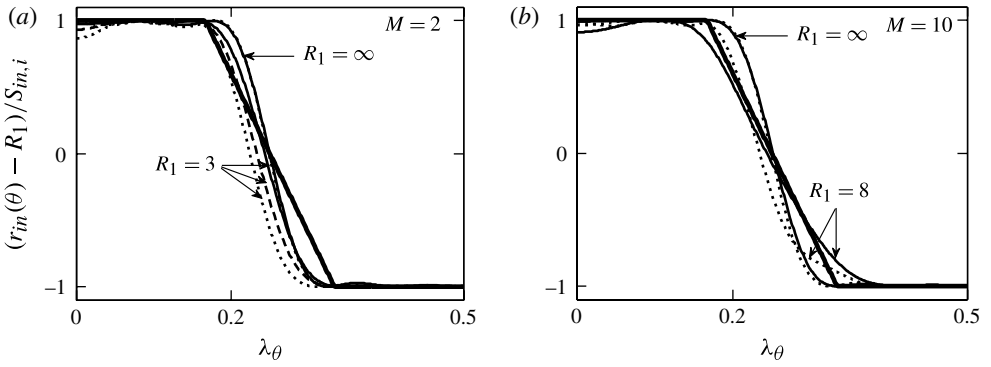


FIGURE 17. Evolution of the optimal shape of $M = 2, 10$ equal-depth grooves placed at the inner cylinder as a function of the wall curvature R_1. Solid, dashed and dotted lines correspond to the depth of the grooves $S_{in,i} = S_{in,o} = S = 0.2, 0.5, 0.8$, respectively. All these lines overlap for $R_1 = \infty$. The other values of R_1 shown correspond to values close to those that cause a change from drag reduction to a drag increase (see figure 11). Thick lines describe the universal shape, i.e. trapezoid with $a = b = \lambda/6$ and $c = d = \lambda/3$ (see text for details).

$S_{in,i} = S_{in,o} = S = 0.2, 0.5, 0.8$, is illustrated in figure 17. Variations of the shape are fairly minor and, thus, it is possible to propose a universal shape that well approximates the optimal grooves over a wide range of parameters. This universal shape has the form of a trapezoid characterized by $a = b = \lambda/6$ and $c = d = \lambda/3$ (see figure 6 for definition of parameters). The deviations from the universal shape increase with an increase of the depth of the cut and reduction of R_1. The largest deviations correspond to the wavenumber $\alpha = M/R_1$ approaching its critical value (see figure 11) where the grooves begin to generate additional drag. Availability of the universal shape provides a general answer to the optimization problem which eliminates the need for detailed analysis if the associated error is viewed as acceptable.

Replacement of the optimal shape by the universal trapezoid may lead to an error in the determination of the modification friction factor. Comparisons of the actual optimal modification friction factor and the modification friction factor for the universal trapezoid displayed in figure 18 demonstrate that this error is negligible in most practical applications. This error may become excessive when R_1 becomes small as the difference between the actual optimal shape and the universal trapezoid becomes excessive (see figure 16). Such configurations are likely to be of marginal interest as they correspond to the wavenumber $\alpha = M/R_1$ approaching its critical value and, thus, produce marginal reductions of pressure loss.

Figure 19 illustrates variations of the modification friction factor for the optimal grooves approximated using the universal trapezoid over the whole range of groove amplitudes S and wall curvature R_1 of practical interest. These data provide information regarding the maximum potential drag reduction that can be produced by the grooves. The same figure also displays results for grooves described by one Fourier mode. The difference illustrates the potential gains due to the replacement of the simple sinusoidal grooves by the optimal grooves. It can be seen that this difference is generally smaller than 10 % which supports the conclusions discussed in § 5.2 and illustrates the power of the reduced-order model.

https://doi.org/10.1017/jfm.2012.547 Published online by Cambridge University Press

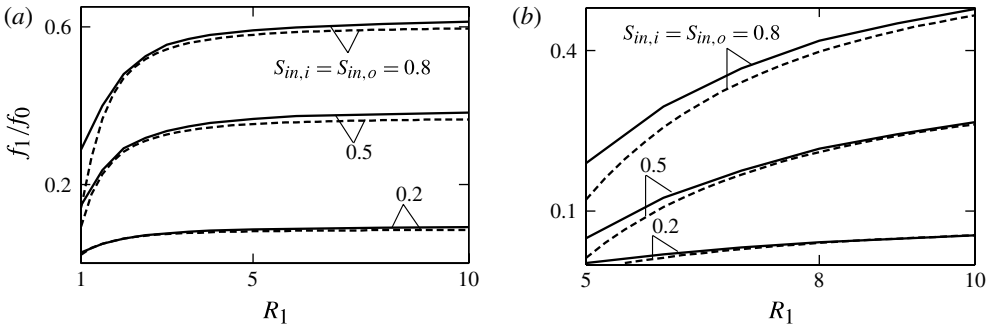


FIGURE 18. Variation of the normalized modification friction factor f_1/f_0 for (*a*) $M = 2$ and (*b*) $M = 10$ equal-depth optimal grooves placed on the inner cylinder (solid lines). Dashed lines show the modification friction factors for the same grooves approximated using the universal trapezoid. See text for details.

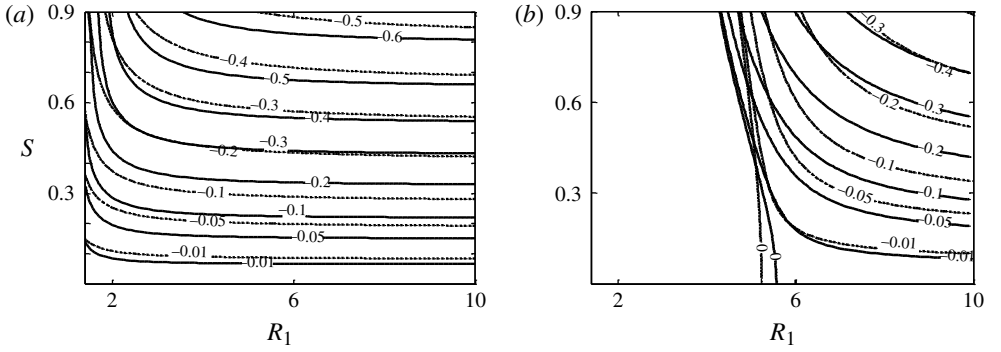


FIGURE 19. Variation of the normalized modification friction factor f_1/f_0 as a function of the wall curvature R_1 and the groove amplitude $S_{in,i} = S_{in,o} = S$ for (*a*) $M = 2$ and (*b*) $M = 10$ universal equal-depth trapezoidal grooves placed on the inner cylinder (see text for discussion). Dashed lines are for the sinusoidal grooves defined by (5.4) with $S_{ave,out} = S_{ave,in} = 0$.

Consider similar grooves added to the outer cylinder while the inner cylinder is kept smooth. Constraint (6.4) is replaced by

$$\max_\theta |r_{in}(\theta)| = \min_\theta |r_{in}(\theta)| = R_1, \tag{6.6a,b}$$

$$\max_\theta |r_{out}(\theta)| = 1 + R_1 + S_{out,o}, \quad \min_\theta |r_{out}(\theta)| = 1 + R_1 - S_{out,i}, \quad S_{out,i} = S_{out,o} \tag{6.6c–e}$$

where $S_{out,i}$ and $S_{out,o}$ stand for the height and the depth of the groove, respectively. An analysis similar to that carried out in the case of grooves placed on the inner cylinder results in similar conclusions. Deviations from the universal shape (not shown) are, however, much smaller as the effective wavenumber $\alpha = M/(1 + R_1)$ is smaller.

The general case corresponds to grooves placed on both cylinders, i.e. the constraints take the form

$$\max_\theta |r_{in}(\theta)| = R_1 + S_{in,o}, \quad \min_\theta |r_{in}(\theta)| = R_1 - S_{in,i}, \quad S_{in,i} = S_{in,o}, \tag{6.7a–c}$$

$$\max_\theta |r_{out}(\theta)| = 1 + R_1 + S_{out,o}, \quad \min_\theta |r_{out}(\theta)| = 1 + R_1 - S_{out,i}, \quad S_{out,i} = S_{out,o}. \tag{6.7d–f}$$

https://doi.org/10.1017/jfm.2012.547 Published online by Cambridge University Press

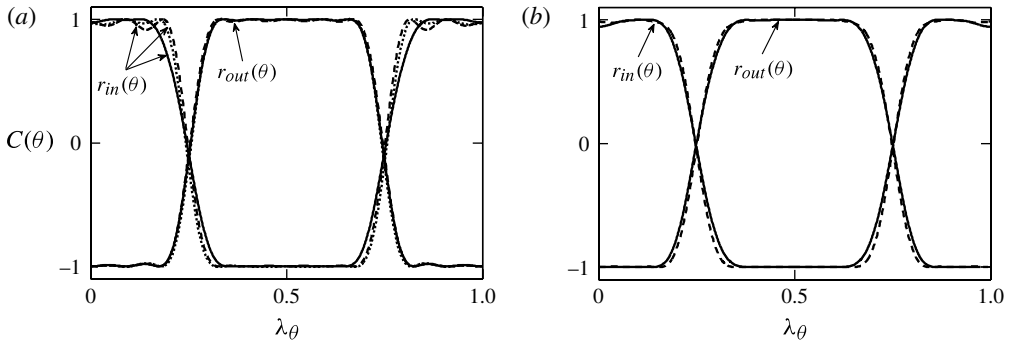


FIGURE 20. Optimal shapes of the equal-depth grooves placed on both cylinders. $C(\theta)$ is defined as $[r_{out}(\theta) - 1 - R_1]/S_{out,i}$, $[r_{in}(\theta) - R_1]/S_{in,i}$. (*a*) $M = 2$ grooves; the solid lines are for $R_1 = 3$, $S_{in,o} = S_{in,i} = S_{out,o} = S_{out,o} = 0.2$, the dotted lines are for $R_1 = 5$, $S_{in,o} = S_{in,i} = S_{out,o} = S_{out,o} = 0.4$, and the dashed lines are for $R_1 = 10$, $S_{in,o} = S_{in,i} = S_{out,o} = S_{out,o} = 0.4$. (*b*) displays results for $M = 10$ grooves; the solid lines are for $R_1 = 8$, $S_{in,o} = S_{in,i} = S_{out,o} = S_{out,o} = 0.2$, and the dashed lines are for $R_1 = 10$ and $S_{in,o} = S_{in,i} = S_{out,o} = S_{out,o} = 0.4$.

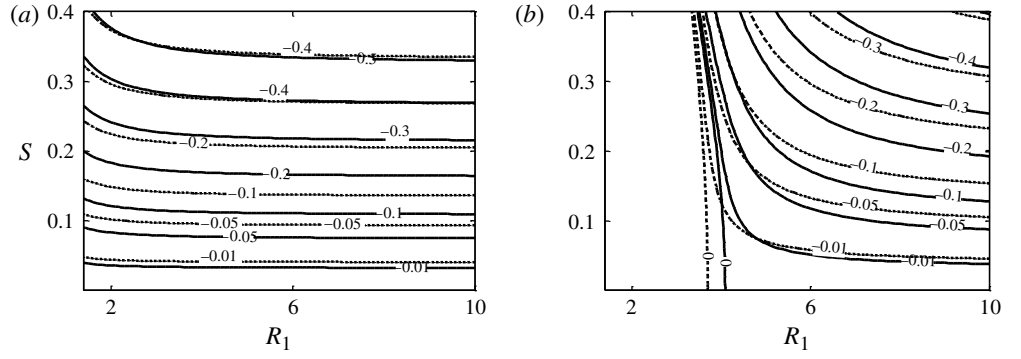


FIGURE 21. Variations of the normalized modification friction factor f_1/f_0 as a function of the wall curvature R_1 and the groove amplitude $S_{in,i} = S_{in,o} = S_{out,i} = S_{out,o} = S$ for (*a*) $M = 2$ and (*b*) $M = 10$ universal equal-depth trapezoidal grooves placed on both cylinders (see text for discussion). Dashed lines are for the sinusoidal grooves defined by (5.4) with $S_{ave,out} = S_{ave,in} = 0$. Note that the universal trapezoid does not offer a good approximation for the optimal grooves under conditions close to transition between the drag-increasing and the drag-decreasing geometries.

The results displayed in figure 20 demonstrate that the shapes of the optimal grooves are nearly the same as the shapes of the grooves determined for each cylinder separately, and the grooves on the outer cylinder are shifted with respect to those at the inner cylinder by a half wavelength in the axial direction. The results displayed in figure 21 show that the drag reduction produced by these grooves, with shapes approximated using the universal trapezoid, is approximately equal to the drag reduction produced by grooves placed only on one cylinder but with a double amplitude (compare figures 19 and 21). Figure 21 also presents results for simple sinusoidal grooves placed on both cylinders. It can be seen that such grooves produce $\sim$10 % less drag reduction than the optimal grooves. The reader should recall, when

https://doi.org/10.1017/jfm.2012.547 Published online by Cambridge University Press

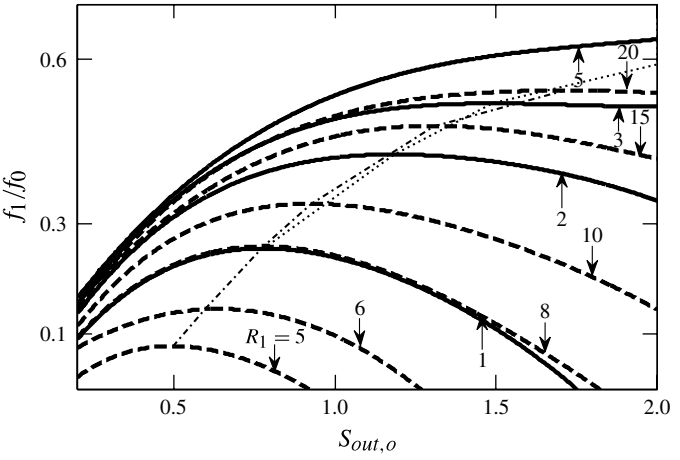


FIGURE 22. Variation of the normalized modification friction factor f_1/f_0 as a function of the depth of the groove, i.e. $S_{out,o}$, for the unequal-depth grooves. The grooves are placed on the outer cylinder and have the same maximum height set at $S_{out,i} = 0.5$. Solid and dashed lines correspond to the use of $M = 2$ and $M = 10$ grooves, respectively. The dotted ($M = 2$) and dashed–dotted ($M = 10$) lines identify the depth of the groove that leads to the maximum drag reduction.

reviewing these results, that predictions based on the universal trapezoid are not accurate when the groove wavenumber is close to its critical value.

6.2. *Unequal-depth grooves*

Consider grooves with unequal depth which are initially placed only on the outer cylinder. The maximum depth and the maximum height of the groove are not the same but, as before, they are specified by the user. Such grooves correspond to constraints in the form

$$\max_\theta |r_{out}(\theta)| = 1 + R_1 + S_{out,o}, \quad \min_\theta |r_{out}(\theta)| = 1 + R_1 - S_{out,i}, \tag{6.8a,b}$$

where the values of $S_{out,o}$ and $S_{out,i}$ are different and known. The constraints (6.8) need to be supplemented by the constraint expressing the need to maintain the constant flow cross-sectional area.

Variations of the modification friction factor, when the height of the groove is fixed at $S_{out,i} = 0.5$ while the depth $S_{out,o}$ is varied, are displayed in figure 22. It can be seen that there exists a depth that leads to the largest drag reduction. We shall refer to this depth as the optimal depth D_{opt} which, together with the corresponding shape, determines the optimal geometry. Variations of the shape of the optimal grooves as a function of $S_{out,o}$ are illustrated in figure 23. For small enough $S_{out,o}$ this shape looks like the universal trapezoid discussed in the previous section. A sufficient increase of $S_{out,o}$ leads to a shape that resembles a delta function. The shape that gives the largest drag reduction can be approximated by the delta function, which underlines the universality of the optimal geometry.

The optimal geometry can be determined directly by limiting the constraint to the following form:

$$\min_\theta |r_{out}(\theta)| = 1 + R_1 - S_{out,i}, \tag{6.9}$$

https://doi.org/10.1017/jfm.2012.547 Published online by Cambridge University Press

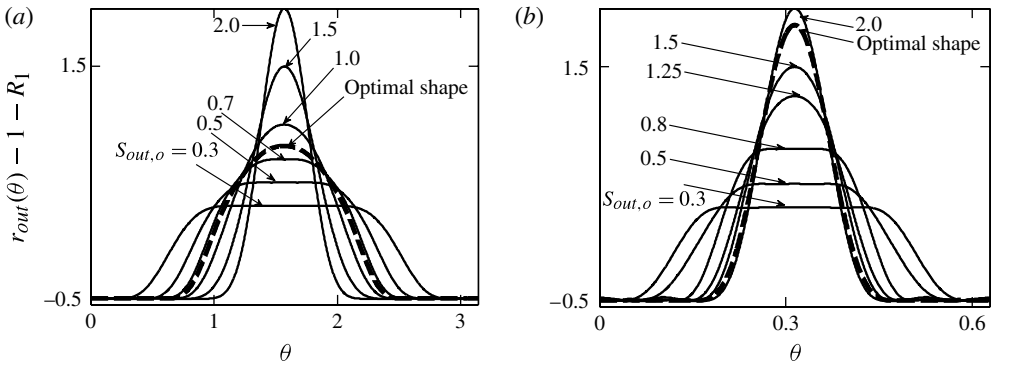


FIGURE 23. Evolution of the optimal shape of unequal-depth grooves placed on the outer cylinder as a function of the depth of the groove $S_{out,o}$. The height of the groove is set at $S_{out,i} = 0.5$. (*a*) $M = 2$, $R_1 = 1$, and (*b*) $M = 10$, $R_1 = 20$. Dashed lines illustrate shapes corresponding to the optimal depth.

and treating the depth of the groove $S_{out,o}$ as an unknown. Evolution of the optimal geometry is illustrated in figure 24(*a,b*) where the groove height has been scaled with its maximum. Rescaling of the width of the groove with its width at half-height W_{half} leads to universal shapes displayed in figure 24(*c,d*). These shapes are well approximated by a delta function in the form $y = \exp(-3.2x^2)$. The complete information about the optimal geometry consists of the universal delta function, and the values of W_{half} and D_{opt} displayed in figure 25(*b,c*). Figure 25(*a*) provides information about the drag reduction that can be produced by the optimal geometry. In general, an increase in the number of grooves M reduces the drag reduction as well as the optimal depth and the width of the grooves. While it is difficult to make direct comparisons between the optimal geometry and the simple sinusoidal grooves, the former generate a drag reduction that is up 50 % higher than the latter.

Analysis of the same grooves placed on the inner cylinder leads to very similar conclusions regarding the optimal shape, the optimal depth and the optimal geometry. These results are, therefore, not presented. Figure 26 illustrates the properties of the optimal geometry made up of grooves placed on both cylinders as well as the resulting drag reduction. Grooves on the outer cylinder are shifted by a half-wavelength in the axial direction with respect to those on the inner cylinder. The grooves have shapes similar to those found in the case of only one grooved cylinder. The drag reduction is approximately twice the drag reduction obtained using grooves with the same height placed on only one cylinder.

7. Conclusions

A systematic analysis of the variations of the pressure gradients required to maintain laminar flows through annuli fitted with longitudinal grooves has been carried out. The main objective of the analysis was the identification of the forms of the grooves that result in the reduction of the pressure gradient below the level needed to maintain the same flow rate as in a smooth annuli, i.e. identification of the form of the drag-reducing grooves. It has been demonstrated that the groove-induced changes in the pressure drop can be represented as a superposition of a pressure drop due to

https://doi.org/10.1017/jfm.2012.547 Published online by Cambridge University Press

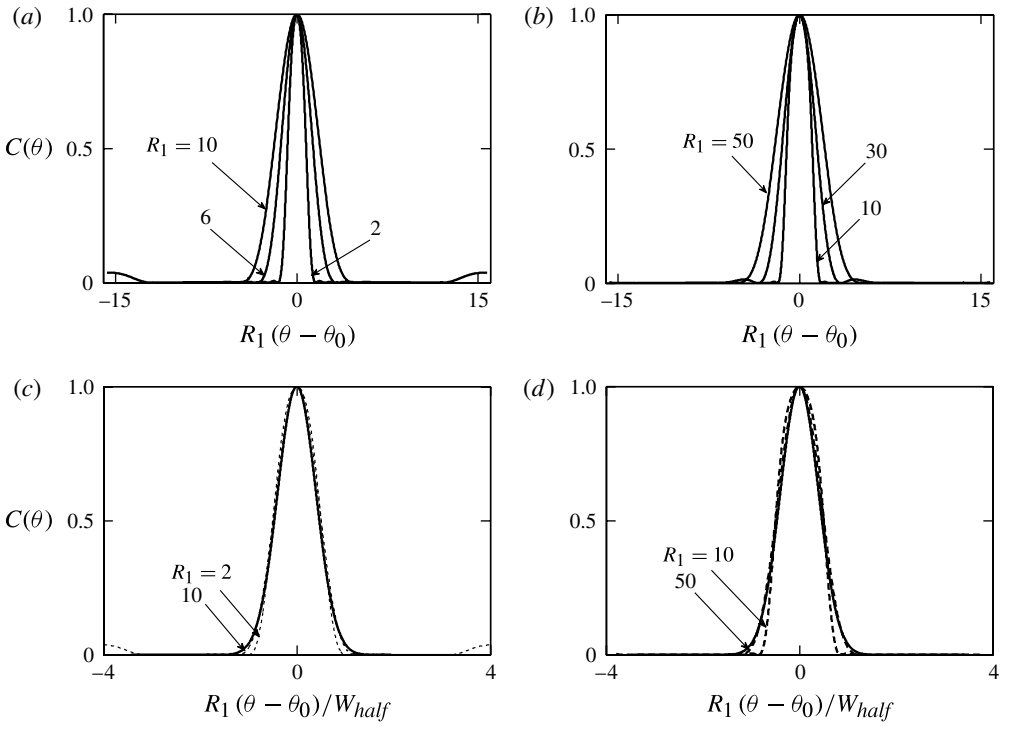


FIGURE 24. Shapes of unequal-depth optimal grooves corresponding to the optimal depth, i.e. the optimal geometry, for grooves placed on the outer cylinder for selected values of the wall curvature R_1. $C(\theta)$ is defined as $[r_{out}(\theta) - (r_{out})_{min}]/[(r_{out})_{max} - (r_{out})_{min}]$. The height of the groove is set at $S_{out,i} = 0.5$. (*a*) $M = 2$ and (*b*) $M = 10$. (*c,d*) The same shapes, but normalized with the width at half-height W_{half}. The universal shape has the form of a delta function defined by $y = \exp(-3.2x^2)$ and is illustrated using solid lines.

a change in the average position of the bounding cylinders and a pressure drop due to flow modulations induced by the shape of the grooves. The former effect can be evaluated analytically while the latter requires explicit computations.

Detailed analysis of the modulation effects has been carried out. It has been demonstrated that a reduced-order model is an effective tool for the extraction of features of groove geometry that are relevant to the drag generation. In the case of equal-depth grooves, one Fourier mode from the Fourier expansion representing the annulus geometry is sufficient to predict pressure losses with an accuracy sufficient for most applications. The maximum depth and the maximum height are the same for such grooves. It is shown that the presence of the grooves may lead to a reduction of pressure loss in spite of an increase of the surface wetted area. The drag-decreasing grooves are characterized by the groove wavenumber M/R_1 being smaller than a certain critical value, where M denotes the number of grooves being used and R_1 stands for the radius of the annulus; this number marginally depends on the groove amplitude and does not depend on the flow Reynolds number. It is shown that the drag reduction mechanism relies on a re-arrangement of the bulk flow that leads to the largest mass flow taking place in the area of the largest annulus opening.

https://doi.org/10.1017/jfm.2012.547 Published online by Cambridge University Press

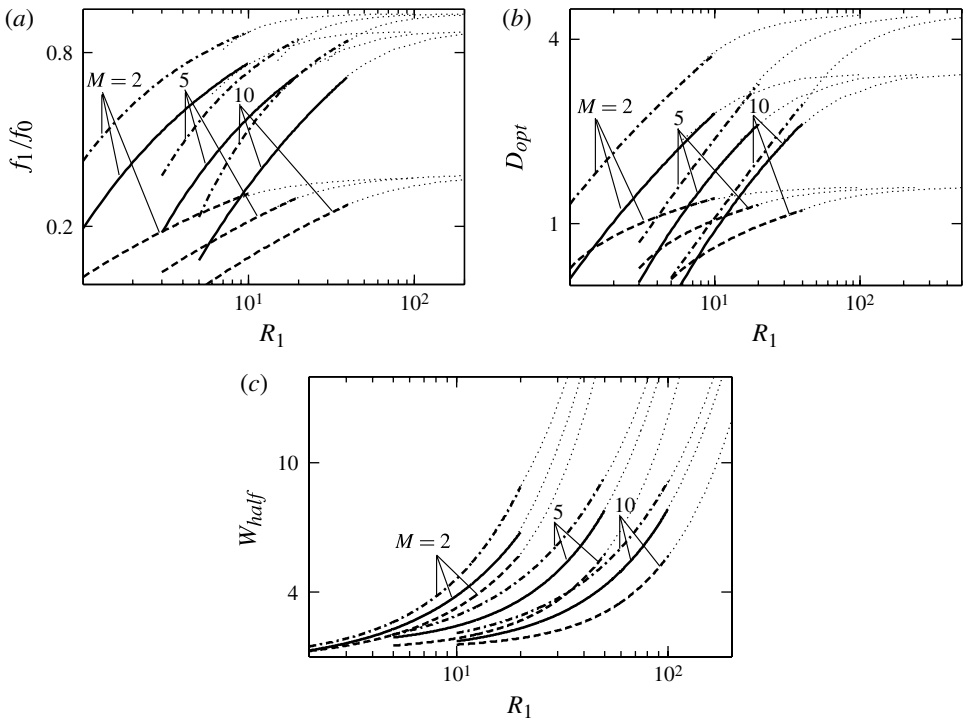


FIGURE 25. Variations of the normalized modification friction factor (*a*), the optimal depth (*b*) and the half-width of the optimal groove (*c*) as a function of the wall curvature R_1 for an annulus with a smooth inner cylinder and the optimal geometry of the outer cylinder. The maximum heights of the grooves are set as $S_{out,i} = 0.8$ (dashed–dotted lines), $S_{out,i} = 0.5$ (solid lines) and $S_{out,i} = 0.2$ (dashed lines). Dotted lines correspond to the asymptotic solution, i.e. $R_1 \to \infty$.

A search for the form of the grooves that results in the largest decrease of the drag, i.e. the optimal shape, has been carried out. The reduced-order model involving 3–4 Fourier modes is able to capture drag-reducing characteristics of such grooves with an accuracy sufficient for most applications. It is shown that the form of the optimal grooves depends on the constraints. Detailed analysis has been carried out for two classes of constraints, i.e. equal-depth grooves and unequal-depth grooves.

It has been found that in the case of equal-depth grooves the optimal shape changes very little as a function of the flow and geometry parameters and can be approximated using a special form of trapezoid. The error of such an approximation is generally negligible unless the geometry parameters place the groove close to the boundary that separates the drag-reducing grooves from the drag-increasing grooves. The optimal grooves have nearly the same form regardless of whether they are placed on the inner or outer cylinders. The most effective placement of the grooves on both cylinders corresponds to a half-wavelength shift in the axial direction between the two sets of grooves, with their shapes being nearly identical to those found in the case of annuli with only one grooved cylinder. Approximately the same drag reduction is produced by fitting one cylinder with grooves having an amplitude that is twice those placed on both cylinders.

https://doi.org/10.1017/jfm.2012.547 Published online by Cambridge University Press

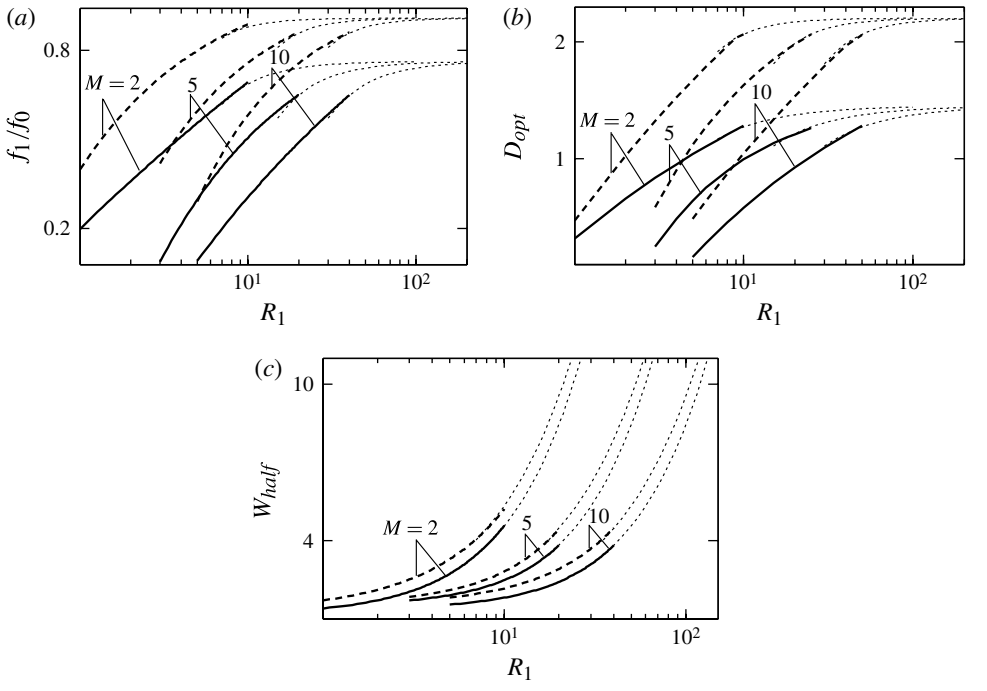


FIGURE 26. Variations of the normalized modification friction factor (*a*), the optimal depth (*b*) and the half-width of the optimal groove (*c*) as a function of the wall curvature R_1 for an annulus with the optimal geometries of the inner and outer cylinders. The maximum heights of the grooves on the inner and outer cylinders are the same and set at the level of $S_{out,i} = 0.4$ (dashed lines) and $S_{out,i} = 0.2$ (solid lines). Dotted lines correspond to the asymptotic solution, i.e. $R_1 \to \infty$.

Drag reduction is a non-monotonic function of groove depth in the case of the unequal-depth grooves. In this case, the maximum height and the maximum depth of the groove are not the same. The depth that gives the largest drag reduction for a given height, the optimal depth, as well as the corresponding groove shape define the optimal geometry. The properties of the optimal geometry can be determined directly through the optimization process. It is shown that the optimal shape forming the optimal geometry can be approximated using a delta function. The maximum possible drag reduction, corresponding to the optimal geometry, has been determined for a range of parameters of practical interest. It is shown that this reduction is significantly larger than the reduction associated with the equal-depth grooves. The optimal geometry is nearly the same for the outer and inner cylinders. Placement of grooves on both cylinders produces the largest drag reduction when they are shifted with respect to each other by a half-wavelength in the axial direction.

The above predictions apply to laminar flows only. Stability analysis is required in order to determine the range of Reynolds numbers where laminar flows exist. The predicted pressure losses need to be confirmed experimentally.

Acknowledgement

This work has been carried out with the support of NSERC of Canada.

https://doi.org/10.1017/jfm.2012.547 Published online by Cambridge University Press

Appendix A

This appendix gives an explicit form of coefficients appearing in (3.6):

$$\left.\begin{aligned} F_{A,1} &= \frac{R_1^{-1}H_1(\eta,\xi)}{1+F(\eta,\xi)/R_1}+\frac{H_3(\eta,\xi)}{[1+F(\eta,\xi)/R_1]^2},\\ F_{A,2} &= H_1^2(\eta,\xi)+\frac{H_2^2(\eta,\xi)}{[1+F(\eta,\xi)/R_1]^2},\\ F_{A,3} &= \frac{2\alpha H_2(\eta,\xi)}{[1+F(\eta,\xi)/R_1]^2}, \quad F_{A,4}=\frac{\alpha^2}{[1+F(\eta,\xi)/R_1]^2}, \end{aligned}\right\} \tag{A 1}$$

$$H_1(\eta,\xi)=2f^{-1}(\xi), \tag{A 2}$$

$$H_2(\eta,\xi)=-\alpha\left\{[y_{out}(\xi)+y_{in}(\xi)]_\xi+\eta f_\xi(\xi)\right\}f^{-1}(\xi), \tag{A 3}$$

$$H_3(\eta,\xi)=-\alpha^2\left\{[y_{out}(\xi)+y_{in}(\xi)]_{\xi\xi}+\eta f_{\xi\xi}(\xi)+2\alpha^{-1}H_2(\eta,\xi)f_\xi(\xi)\right\}f^{-1}(\xi), \tag{A 4}$$

$$F(\eta,\xi)=[\eta f(\xi)+y_{out}(\xi)+y_{in}(\xi)]/2, \quad f(\xi)=y_{out}(\xi)-y_{in}(\xi). \tag{A 5}$$

Coefficients (A 2)–(A 5) simplify in the case of geometry described by (3.7) (sinusoidal grooves placed on the inner cylinder) to the form

$$F(\eta,\xi)=1+0.5(\eta-1)f(\xi), \tag{A 6}$$

$$f(\xi)=1-0.5S_{in}\cos\xi, \tag{A 7}$$

$$H_1(\eta,\xi)=2f^{-1}(\xi), \quad H_2(\eta,\xi)=-0.5\alpha S_{in}\sin\xi(\eta-1)f^{-1}(\xi), \tag{A 8}$$

$$H_3(\eta,\xi)=0.25\alpha^2(\eta-1)f^{-2}(\xi)[S_{in}^2(1+\sin^2\xi)-2S_{in}\cos\xi]. \tag{A 9}$$

Appendix B

This appendix presents an asymptotic solution for $R_1\to\infty$ for an annulus with sinusoidal grooves placed at the outer cylinder (see § 3).

The shape of the annulus is given as

$$r_{in}(\theta)=R_1, \quad r_{out}(\theta)=1+R_1+0.5S_{out}\cos(M\theta), \tag{B 1}$$

and the solution has the form

$$\hat{v}_0(\eta)=(1+3S_{out}^2/8)^{-1}g^2(\xi)(1-\eta^2), \tag{B 2}$$

$$\frac{\partial\hat{p}_0}{\partial z}=-\frac{8}{Re}(1+3S_{out}^2/8)^{-1}, \tag{B 3}$$

$$\begin{aligned}\hat{v}_1(\eta)=&\,g^2(\xi)(1+3S_{out}^2/8)^{-1}(1-\eta^2)[\eta g(\xi)/6\\ &+3S_{out}^2(1+3S_{out}^2/8)^{-1}(1+S_{out}^2/16)/16],\end{aligned} \tag{B 4}$$

$$\frac{\partial\hat{p}_1}{\partial z}=\frac{3S_{out}^2}{2Re}(1+3S_{out}^2/8)^{-2}(1+S_{out}^2/16), \tag{B 5}$$

where

$$g(\xi)=1+0.5S_{out}\cos(\xi). \tag{B 6}$$

https://doi.org/10.1017/jfm.2012.547 Published online by Cambridge University Press

Appendix C

This appendix presents components of the stress tensor at the inner cylinder expressed in terms of the discretized variables (see § 4.3):

$$\tau_{rz} = -Re^{-1}B(\xi)^{-1}\sum_{n=-N_M}^{N_M}\sum_{k=0}^{N_T} G_k^{(n)} DT_k(-1)\mathrm{e}^{\mathrm{i}nM\xi}, \tag{C 1}$$

$$\tau_{\theta z} = -Re^{-1}r_{in}(\xi)^{-1}\left[G_2(\xi,-1)\sum_{n=-N_M}^{N_M}\sum_{k=0}^{N_T} G_k^{(n)} DT_k(-1)\mathrm{e}^{\mathrm{i}nM\xi} + \sum_{n=-N_M}^{N_M}\sum_{k=0}^{N_T} \mathrm{i}nMG_k^{(n)}(-1)^k\,\mathrm{e}^{\mathrm{i}nM\xi}\right]. \tag{C 2}$$

The expression for the shear stress along the surface of the cylinder takes the form

$$\begin{aligned} \mathrm{d}F_{total,z} = {} & \left\{1+\left[\left(\sum_{n=-N_A}^{N_A}\mathrm{i}nMH_{in}^{(n)}\mathrm{e}^{\mathrm{i}nM\xi}\right)r_{in}(\xi)^{-1}\right]^2\right\}^{-1/2} \\ & \times\left\{-Re^{-1}r_{in}(\xi)^{-2}\left[G_2(\xi,-1)\sum_{n=-N_M}^{N_M}\sum_{k=0}^{N_T} G_k^{(n)} DT_k(-1)\mathrm{e}^{\mathrm{i}nM\xi} + \sum_{n=-N_M}^{N_M}\sum_{k=0}^{N_T}\mathrm{i}nMG_k^{(n)}(-1)^k\,\mathrm{e}^{\mathrm{i}nM\xi}\right]\right. \\ & \left.\sum_{n=-N_A}^{N_A}\mathrm{i}nMH_{in}^{(n)}\mathrm{e}^{\mathrm{i}nM\xi} + Re^{-1}B(\xi)^{-1}\sum_{n=-N_M}^{N_M}\sum_{k=0}^{N_T} G_k^{(n)} DT_k(-1)\mathrm{e}^{\mathrm{i}nM\xi}\right\}. \end{aligned} \tag{C 3}$$

REFERENCES

ASAI, M. & FLORYAN, J. M. 2006 Experiments on the linear instability of flow in a wavy channel. *Eur. J. Mech. (*B/*Fluids*) **25**, 971–986.

BECHERT, D. W. & BARTENWERFER, M. 1989 The viscous flow on surfaces with longitudinal ribs. *J. Fluid Mech.* **206**, 105–129.

BECHERT, D. W., BRUSE, M., HAGE, W., VAN DER HOEVEN, J. G. T. & HOPPE, G. 1997 Experiments on drag-reducing surfaces and their optimization with an adjustable geometry. *J. Fluid Mech.* **338**, 59–87.

COLEMAN, T. F. & LI, Y. 1994 On the convergence of reflective Newton method for large-scale nonlinear minimization subject to bounds. *Math. Prog.* **67**, 189–224.

COLEMAN, T. F. & LI, Y. 1996 An interior, trust region approach to nonlinear minimization subject to bounds. *SIAM J. Optim.* **6**, 418–445.

COTRELL, D. L. & PEARLSTEIN, A. L. 2006 Linear stability of spiral and annular Poiseuille flow for small radius ratio. *J. Fluid Mech.* **547**, 1–20.

DARCY, H. 1857 *Recherches Expérimentales Relatives au Mouvement de l'Eau dans les Tuyaux*. Mallet-Bachelier.

DOU, H.-S. 2011 Physics of flow instability and turbulent transition in shear flows. *Intl J. Phys. Sci.* **6** (6), 1411–1425.

DOU, H. S., KHOO, B. C. & TSAI, H. M. 2010 Determining the critical conditions of turbulent transition in a fully developed annulus flow. *J. Petrol. Sci. Engng* **73**, 41–47.

https://doi.org/10.1017/jfm.2012.547 Published online by Cambridge University Press

FLORYAN, J. M. 1997 Stability of wall-bounded shear layers in the presence of simulated distributed surface roughness. *J. Fluid Mech.* **335**, 29–55.

FLORYAN, J. M. 2002 Centrifugal instability of Couette flow over a wavy-wall. *Phys. Fluids* **14**, 312–322.

FLORYAN, J. M. 2003 Vortex instability in a diverging–converging channel. *J. Fluid Mech.* **482**, 17–50.

FLORYAN, J. M. 2005 Two-dimensional instability of flow in a rough channel. *Phys. Fluids* **17**, 044101.

FLORYAN, J. M. 2007 Three-dimensional instabilities of laminar flow in a rough channel and the concept of hydraulically smooth wall. *Eur. J. Mech. (*B/*Fluids*) **26**, 305–329.

FLORYAN, J. M. & ASAI, M. 2011 On the transition between distributed and isolated surface roughness and its effect on the stability of channel flow. *Phys. Fluids* **23**, 104101.

FLORYAN, J. M. & FLORYAN, C. 2010 Traveling wave instability in a diverging–converging channel. *Fluid Dyn. Res.* **42**, 025509.

FREAI, CH., LÜSCHER, P. & WINTERMANTEL, W. 2000 Thread-annular flow in vertical pipes. *J. Fluid Mech.* **410**, 185–210.

FROHNAPFEL, B., JOVANOVIĆ, J. & DELGADO, A. 2007 Experimental investigations of turbulent drag reduction by surface-embedded grooves. *J. Fluid Mech.* **590**, 107–116.

GAMRAT, G., FAVRE-MARINET, M., LE PERSON, S., BAVIÉRE, R. & AYELA, F. 2008 An experimental study and modeling of roughness effects on laminar flow in microchannels. *J. Fluid Mech.* **594**, 399–423.

GARCIA-MAYORAL, R. & JIMENEZ, J. 2011 Hydrodynamic stability and breakdown of the viscous regime over riblets. *J. Fluid Mech.* **678**, 317–347.

HAGEN, G. 1854 Uber den Einfluss der Temperatur auf die Bewegung des Wasser in Röhren. *Math. Abh. Akad. Wiss.* **17**.

HEATON, C. J. 2008 Linear instability of annular Poiseuille flow. *J. Fluid Mech.* **610**, 391–406.

HERWIG, H., GLOSS, D. & WENTERODT, T. 2008 A new approach to understanding and modelling the influence of wall roughness on friction factors for pipe and channel flows. *J. Fluid Mech.* **613**, 35–53.

JIMENEZ, J. 2004 Turbulent flows over rough walls. *Annu. Rev. Fluid Mech.* **36**, 173–196.

JUNG, Y. C. & BHUSHAN, B. 2010 Biomimetic structures for fluid drag reduction in laminar and turbulent flows. *J. Phys.: Condens. Matter* **22**, 035104 1–9.

LUCINI, P., MANZO, F. & POZZI, A. 1991 Resistance of grooved surface to parallel flow and cross-flow. *J. Fluid Mech.* **228**, 87–109.

MOHAMMADI, A. & FLORYAN, J. M. 2011 Pressure losses in grooved channels. *Expert Systems in Fluid Dynamics Research Laboratory Rep.* ESFD-4/2011. Department of Mechanical and Materials Engineering, The University of Western Ontario.

MOHAMMADI, A. & FLORYAN, J. M. 2012 Mechanism of drag generation by surface corrugation. *Phys. Fluids* **24**, 013602.

MOODY, L. F. & PRINCETON, N. J. 1944 Friction factors for pipe flow. *Trans. ASME* **66**, 671–684.

MORADI, H. V. & FLORYAN, J. M. 2012 Algorithm for analysis of flows in ribbed annuli. *Intl J. Numer. Meth. Fluids* **68**, 805–838.

MORINI, G. L. 2004 Single-phase convective heat transfer in microchannels: a review of experimental results. *Intl J. Therm. Sci.* **43**, 631–651.

MORKOVIN, M. V. 1990 On roughness-induced transition: facts, views and speculations. In *Instability and Transition* (ed. M. Y. Hussaini & R. G. Voigt). *ICASE/NASA LARC Series*, vol. 1, pp. 281–295. Springer.

NIKURADSE, J. 1933 Strömungsgesetze in Rauhen Rohren. *VDI-Forschungscheft* 361; also *NACA TM* 1292 (1950).

NYE, J. F. 1969 A calculation on the sliding of ice over a wavy surface using a Newtonian viscous approximation. *Proc. R. Soc.Lond.* A **311**, 445–467.

PAPAUTSKY, I., BRAZZLE, J., AMEEL, T. & FRAZIER, A. B. 1999 Laminar fluid behavior in microchannels using micropolar fluid theory. *Sensors Actuators* A **73**, 101–108.

https://doi.org/10.1017/jfm.2012.547 Published online by Cambridge University Press

REYNOLDS, O. 1883 An experimental investigation of the circumstances which determine whether the motion of water shall be direct or sinuous, and of the law of resistance in parallel channels. *Phil. Trans. R. Soc. Lond.* **174**, 935–982.

SARIC, W. S., CARRILLO, R. B. & REIBERT, M. S. 1998 Nonlinear stability and transition in 3-D boundary layers. *Meccanica* **33**, 469–487.

SCHLICHTING, H. 1979 *Boundary Layer Theory*, 7th edn. McGraw-Hill.

SHARP, K. V. & ADRIAN, R. J. 2004 Transition from laminar to turbulent flow in liquid filled microtubes. *Exp. Fluids* **36**, 741–747.

SOBHAN, C. B. & GARIMELLA, S. V. 2001 A comparative analysis of studies on heat transfer and fluid flow in microchannels. *Microscale Therm. Engng* **5**, 293–311.

SZUMBARSKI, J. & FLORYAN, J. M. 2006 Transient disturbance growth in a corrugated channel. *J. Fluid Mech.* **568**, 243–272.

TASOS, C. P., GEORGIOS, C. G. & ANDREAS, N. A. 1999 *Viscous Fluid Flow*. CRC.

VALDES, J. R., MIANA, M. J., PELEGAY, J. L., NUNEZ, J. L. & PÜTZ, T. 2007 Numerical investigation of the influence of roughness on the laminar incompressible fluid flow through annular microchannels. *Intl J. Heat Mass Transfer* **50**, 1865–1878.

WALTON, A. G., LABADIN, J. & YIONG, S. P. 2010 Axial flow between sliding, non-concentric cylinders with applications to thread injection. *Q. J. Mech. Appl. Maths* **63**, 315–334.

WALSH, M. J. 1980 Drag characteristics of V-groove and transverse curvature riblets. In *Viscous Drag Reduction* (ed. G. R. Hough), vol. 72, pp. 168–184. AIAA.

WALSH, M. J. 1983 Riblets as a viscous drag reduction technique. *AIAA J.* **21**, 485–486.

https://doi.org/10.1017/jfm.2012.547 Published online by Cambridge University Press